- The Dynamics of Ions on Phased Radio-frequency Carpets in High Pressure
- 2 Gases and Application for Barium Tagging in Xenon Gas Time Projection
 Chambers

B.J.P. Jones^{c,*}, A. Raymond^c, K. Woodruff^{c,*}, N. Byrnes^c, A.A. Denisenko^d, F.W. Foss^d, K. Navarro^c,

```
D.R. Nygren<sup>c,1</sup>, T.T. Vuong<sup>d</sup>, C. Adams<sup>b</sup>, H. Almazán<sup>k</sup>, V. Álvarez<sup>z</sup>, B. Aparicio<sup>x</sup>, A.I. Aranburu<sup>v</sup>,
                       L. Arazi<sup>g</sup>, I.J. Arnquist<sup>t</sup>, S. Ayet<sup>p</sup>, C.D.R. Azevedo<sup>e</sup>, K. Bailey<sup>b</sup>, F. Ballester<sup>z</sup>,
       J.M. Benlloch-Rodríguez<sup>u</sup>, F.I.G.M. Borges<sup>n</sup>, S. Bounasser<sup>k</sup>, S. Cárcel<sup>s</sup>, J.V. Carrión<sup>s</sup>, S. Cebrián<sup>aa</sup>,
       E. Church<sup>t</sup>, C.A.N. Conde<sup>n</sup>, T. Contreras<sup>k</sup>, F.P. Cossío<sup>u,i</sup>, G. Díaz<sup>y</sup>, J. Díaz<sup>s</sup>, T. Dickel<sup>p</sup>, J. Escada<sup>n</sup>,
       R. Esteve<sup>z</sup>, A. Fahs<sup>k</sup>, R. Felkai<sup>g</sup>, L.M.P. Fernandes<sup>m</sup>, P. Ferrario<sup>u,i</sup>, A.L. Ferreira<sup>e</sup>, E.D.C. Freitas<sup>m</sup>,
                  Z Freixa<sup>v,i</sup>, J. Generowicz<sup>u</sup>, A. Goldschmidt<sup>h</sup>, J.J. Gómez-Cadenas<sup>u,i,1</sup>, R. González<sup>u</sup>,
10
              D. González-Díaz<sup>y</sup>, R. Guenette<sup>k</sup>, R.M. Gutiérrez<sup>j</sup>, J. Haefner<sup>k</sup>, K. Hafidi<sup>b</sup>, J. Hauptman<sup>a</sup>,
11
       C.A.O. Henriques<sup>m</sup>, J.A. Hernando Morata<sup>y</sup>, P. Herrero-Gómez<sup>u,w</sup>, V. Herrero<sup>z</sup>, J. Ho<sup>k</sup>, Y. Ifergan<sup>g</sup>,
12
        M. Kekic<sup>y</sup>, L. Labarga<sup>r</sup>, A. Laing<sup>c</sup>, P. Lebrun<sup>f</sup>, D. Lopez Gutierrez<sup>k</sup>, N. López-March<sup>z</sup>, M. Losada<sup>j</sup>,
               R.D.P. Mano<sup>m</sup>, J. Martín-Albo<sup>s</sup>, A. Martínez<sup>s</sup>, G. Martínez-Lema<sup>g</sup>, M. Martínez-Vara<sup>u,s</sup>,
14
      A.D. McDonald<sup>c</sup>, Z.E. Meziani<sup>b</sup>, K. Mistry<sup>c</sup>, F. Monrabal<sup>u,i</sup>, C.M.B. Monteiro<sup>m</sup>, F.J. Mora<sup>z</sup>, J. Muñoz
15
      Vidal<sup>s</sup>, P. Novella<sup>s</sup>, E. Oblak<sup>u</sup>, M. Odriozola-Gimeno<sup>u</sup>, B. Palmeiro<sup>y,s</sup>, A. Para<sup>f</sup>, J. Pérez<sup>l</sup>, M. Querol<sup>s</sup>,
16
      A.B. Redwine<sup>g</sup>, J. Renner<sup>y</sup>, L. Ripoll<sup>q</sup>, I. Rivilla<sup>u,i</sup>, Y. Rodríguez García<sup>j</sup>, J. Rodríguez<sup>z</sup>, C. Rogero<sup>w</sup>,
17
       L.\ Rogers^c,\ B.\ Romeo^{u,l},\ C.\ Romo-Luque^s,\ F.P.\ Santos^n,\ J.M.F.\ dos\ Santos^m,\ A.\ Sim\'on^g,\ M.\ Sorel^s,
18
         C. Stanford<sup>k</sup>, J.M.R. Teixeira<sup>m</sup>, P. Thapa<sup>d</sup>, J.F. Toledo<sup>z</sup>, J. Torrent<sup>u</sup>, A. Usón<sup>s</sup>, J.F.C.A. Veloso<sup>e</sup>,
19
                                      R. Webb<sup>o</sup>, R. Weiss-Babai<sup>g,2</sup>, J.T. White<sup>o,3</sup>, N. Yahlali<sup>s</sup>
20
                      <sup>a</sup> Department of Physics and Astronomy, Iowa State University, Ames, IA 50011-3160, USA
21
                                           <sup>b</sup> Argonne National Laboratory, Argonne, IL 60439, USA
22
                         <sup>c</sup> Department of Physics, University of Texas at Arlington, Arlington, TX 76019, USA
23
             d Department of Chemistry and Biochemistry, University of Texas at Arlington, Arlington, TX 76019, USA
25
      <sup>e</sup> Institute of Nanostructures, Nanomodelling and Nanofabrication (i3N), Universidade de Aveiro, Campus de Santiago,
                                                              Aveiro, 3810-193, Portugal
26
                                      <sup>f</sup> Fermi National Accelerator Laboratory, Batavia, IL 60510, USA
27
           <sup>9</sup> Nuclear Engineering Unit, Faculty of Engineering Sciences, Ben-Gurion University of the Negev, P.O.B. 653,
28
                                                             Beer-Sheva, 8410501, Israel
29
                    h Lawrence Berkeley National Laboratory (LBNL), 1 Cyclotron Road, Berkeley, CA 94720, USA
                                     Ikerbasque (Basque Foundation for Science), Bilbao, E-48009, Spain
31
      j Centro de Investigación en Ciencias Básicas y Aplicadas, Universidad Antonio Nariño, Sede Circunvalar, Carretera 3
32
                                                        Este No. 47 A-15, Bogotá, Colombia
33
                                 <sup>k</sup> Department of Physics, Harvard University, Cambridge, MA 02138, USA
34
                  Laboratorio Subterráneo de Canfranc, Paseo de los Ayerbe s/n, Canfranc Estación, E-22880, Spain
35
                  <sup>m</sup> LIBPhys, Physics Department, University of Coimbra, Rua Larga, Coimbra, 3004-516, Portugal
36
                            <sup>n</sup> LIP, Department of Physics, University of Coimbra, Coimbra, 3004-516, Portugal
37
               Operation of Physics and Astronomy, Texas A&M University, College Station, TX 77843-4242, USA
38
                            <sup>p</sup> II. Physikalisches Institut, Justus-Liebiq-Universitat Giessen, Giessen, Germany
39
                   ^q\ Escola\ Politècnica\ Superior,\ Universitat\ de\ Girona,\ Av.\ Montilivi,\ s/n,\ Girona,\ E-17071,\ Spain
40
      <sup>r</sup> Departamento de Física Teórica, Universidad Autónoma de Madrid, Campus de Cantoblanco, Madrid, E-28049, Spain
41
      <sup>s</sup> Instituto de Física Corpuscular (IFIC), CSIC & Universitat de València, Calle Catedrático José Beltrán, 2, Paterna,
42
                                                                     E-46980, Spain
                               <sup>t</sup> Pacific Northwest National Laboratory (PNNL), Richland, WA 99352, USA
44
         <sup>u</sup> Donostia International Physics Center, BERC Basque Excellence Research Centre, Manuel de Lardizabal 4, San
45
                                                       Sebastián / Donostia, E-20018, Spain
46
      ^v Department of Applied Chemistry, Universidad del Pais Vasco (UPV/EHU), Manuel de Lardizabal 3, San Sebastián /
47
48
                                                              Donostia, E-20018, Spain
       w Centro de Física de Materiales (CFM), CSIC & Universidad del Pais Vasco (UPV/EHU), Manuel de Lardizabal 5,
49
                                                    San Sebastián / Donostia, E-20018, Spain
50
```

Abstract

51

52

53 54

55

56

57

58

* Department of Organic Chemistry I, University of the Basque Country (UPV/EHU), Centro de Innovación en

Química Avanzada (ORFEO-CINQA), San Sebastián / Donostia, E-20018, Spain

y Instituto Gallego de Física de Altas Energías, Univ. de Santiago de Compostela, Campus sur, Rúa Xosé María Suárez

Núñez, s/n, Santiago de Compostela, E-15782, Spain

^z Instituto de Instrumentación para Imagen Molecular (I3M), Centro Mixto CSIC - Universitat Politècnica de València,

Camino de Vera s/n, Valencia, E-46022, Spain

aa Centro de Astropartículas y Física de Altas Energías (CAPA), Universidad de Zaragoza, Calle Pedro Cerbuna, 12,

Zaragoza, E-50009, Spain

Radio-frequency (RF) carpets with ultra-fine pitches are examined for ion transport in gases at atmospheric pressures and above. We develop new analytic and computational methods for modeling RF ion transport at densities where dynamics are strongly influenced by buffer gas collisions. An analytic description of levitating and sweeping forces from phased arrays is obtained, then thermodynamic and kinetic principles are used to calculate ion loss rates in the presence of collisions. This methodology is validated against detailed microscopic SIMION simulations. We then explore a parameter space of special interest for neutrinoless double beta decay experiments: transport of barium ions in xenon at pressures from 1 to 10 bar. Our computations account for molecular ion formation and pressure dependent mobility as well as finite temperature effects. We discuss the challenges associated with achieving suitable operating conditions, which lie beyond the capabilities of existing devices, using presently available or near-future manufacturing techniques.

1. Introduction

Radio-frequency (RF) carpets and funnels are structures used in mass spectrometry [1, 2] and gasphase stopper cells for nuclear physics [3, 4] that apply a rapidly switching voltage to generate ion levitation and transport in gaseous media. The dynamics of RF levitation are similar to those of a Paul ion trap [5]. In such devices, the applied voltage generates a micro-motion of the trapped ion at the RF frequency. Since the field is non-uniform, at different points in the micro-motion the ion experiences a different strength of electric field. At sufficiently low buffer gas densities the correlation between the electric field strength and position in the micro-cycle generates a time-integrated effective force, even though the time-integrated electric field is zero at every point in space. This force can be associated with a pseudo-potential, as first described by Dehmelt (and is reviewed briefly in the Appendix). A DC "push field" superposed onto the repulsive RF pseudo-potential can then be used to generate a narrow ion trapping region above the carpet surface, along which ions can be transported laterally. The Dehmelt treatment can be applied directly to predict the pseudo-potential for a two-phase RF carpet (shown in Fig. 1, A) since the electric field is sinusoidal in time at every position in space. This calculation has been presented by Schwarz [7], alongside predictions of the corresponding regions of stability for two-phase RF carpets.

Building upon this underlying principle, RF carpets with more complex dynamics have been proposed. Particularly notable is the introduction by Bollen of the ion-surfing scheme [8]. Here, two superposed AC signals are applied across a phased electrode structure. First, a fast RF voltage is applied between adjacent electrode pairs to generate a levitating force via Dehmelt potential; second, a sweeping phased wave at a different frequency is applied over the two-phase RF voltage. This system has ion dynamics that are intractable analytically, and can involve both phase-locked and tumbling ion motions, depending on the surfing frequency. An example of a circuit to realize this system is shown in Fig. 1, B. Simulations of this geometry were performed to explore the regions of stability and dynamics in Ref. [8], which have a nontrivial structure. Demonstrations [9, 10, 11, 12, 13] of ion dynamics on various RF carpet devices based on these modalities have been presented for pressures of up 300 millibar, usually in helium buffer gas.

In this paper we present computational studies of an RF carpet operating mode based on a purely N-phased RF voltage. This device has superficial similarity to the surfing wave system of Bollen, but with a single high frequency phased RF wave responsible for both the levitation and translational dynamics. This operating mode is shown in Fig. 1, C. In this mode the ion trajectories are analytically calculable, and we will show that analytic formulae match well the results detailed microscopic simulations in the widely used SIMION simulation package [14]. Once augmented with stochastic effects, these calculations provide an excellent description of the microscopically simulated RF carpet performance. In this operating mode the same RF wave is responsible for both levitation and transport, simplifying the theoretical treatment and allowing for an analytical solution to the ion motion.

The application that motivates this work is the search for neutrinoless double beta decay in gas-phase ¹³⁶Xe detectors. In such experiments, efficient capture and identification of single barium ions or "barium tagging" [15], is widely understood to be a technology that could offer major advances in experimental

^{*}Corresponding Authors

¹NEXT Co-spokesperson.

²On leave from Soreq Nuclear Research Center, Yavneh, Israel.

³Deceased.

A. Two-phase array with DC sweep field

100

101

102

103

104

107

108

109

111

112

113

115

116

117

119

120

122

123

124

125

126

127

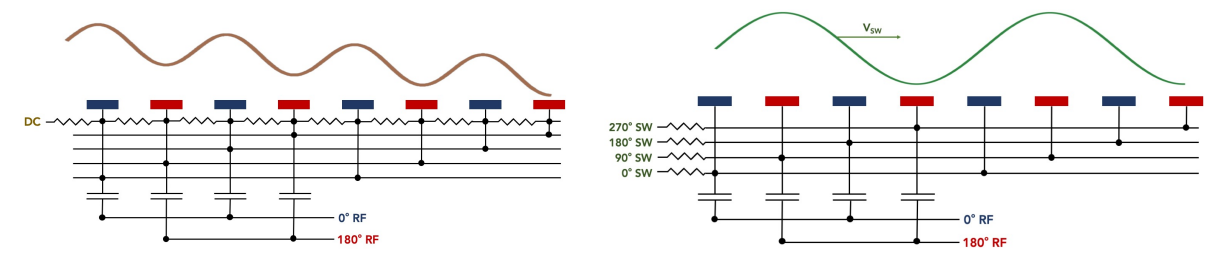
128

130

131

132

B. Surfing-wave array with two RF frequencies



C. N=4 Phased Array

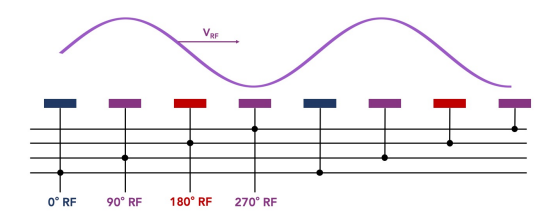


Figure 1: Diagrams showing the drive circuits of three RF carpet configurations: A) two-phase array with DC sweep field, as considered in Ref. [7]; B) superposed two-phase levitation with N-phase surfing wave, as discussed in Ref. [8]; C) N-phased RF array, the subject of the present work.

sensitivity though dramatic reduction of backgrounds from radiogenic and cosmogenic activity. Barium tagging is an area of intense R&D within the neutrinoless double beta decay community [16, 17, 18, 19, 20, 21, 22, 23, 24, 25, 26, 27, 28], and several techniques have now been demonstrated for single barium ion imaging in xenon [29, 20, 22]. Ion collection and extraction from a ton to multi-ton scale volume of liquid or high pressure gas remains major unsolved problem, however [28, 30]. RF-based methods for this purpose have been explored in other contexts. Notably, Ref. [28] proposes to employ gas flow to drive ions through an RF-only funnel for extraction from 10 bar pressure to a vacuum ion trap for atomic fluorescence imaging. Here we explore an alternate approach, the application of ultra-fine pitch RF carpets to the problem of ion transport in dense xenon gas for barium tagging. The required carpets are of similar form to those proposed for ion catching in atmospheric pressure air in Ref [31]. In this scenario, RF transport is implemented without gas flow to sweep barium ions arriving at a detector cathode to a few small single molecule fluorescence sensors [26]. A key goal of this work is to evaluate what operating parameters would need to be achieved to allow for RF transport in high pressure xenon gas experiments, and assess the viability of achieving these beyond-state-of-the-art parameters with available or near-term manufacturing techniques.

The first part of this paper is general in scope, and serves to develop our formalism. Sec. 2 presents analytic calculations of the micro- and macro-trajectories of ion motion on N-phased carpets. We demonstrate that the macro-motion can be considered as driven by a Dehmelt-esque pseudo-potential in the perpendicular direction with a steady sweep force in the transverse. We provide analytic expressions for the levitating force, equilibrium ion height, transverse velocity and micro-motion radius. Sec. 3 compares this calculation, which has idealized point-like electrodes, to a finite element simulation of the electric field and microscopic simulation of smooth ion motion in that geometry. This serves both as a validation of the analytic treatment in the far-field region and a calculation of the distance scales where near-field finite electrode width effects become relevant to ion transport. We find that the analytic calculation is accurate for our purposes at distances above around 0.25 times the RF carpet pitch p, whereas near-field distortions to the electric field due to surface geometry will cause ion losses below $0.25 \times p$. Sec. 4 introduces stochastic effects from collisions. We develop a new thermodynamic approach to predicting ion distributions above RF carpets, and show that the random motion of ions due to collisions can be understood as a thermalization to the buffer gas temperature within the pseudo-potential well. We then provide a kinetic theory derivation of the expected ion loss rates from the tails of this potential into the RF carpet surface. Both predictions are validated against computationally intensive collision-by-collision simulations in SIMION [14]. Sec. 5 explores the transport efficiency of different RF carpet phasings constrained by either fixed peak-to-peak voltage or fixed maximum electrode-to-electrode voltage. In the latter practically important scenario, carpets with 4-6 phases are found to be the most effective.

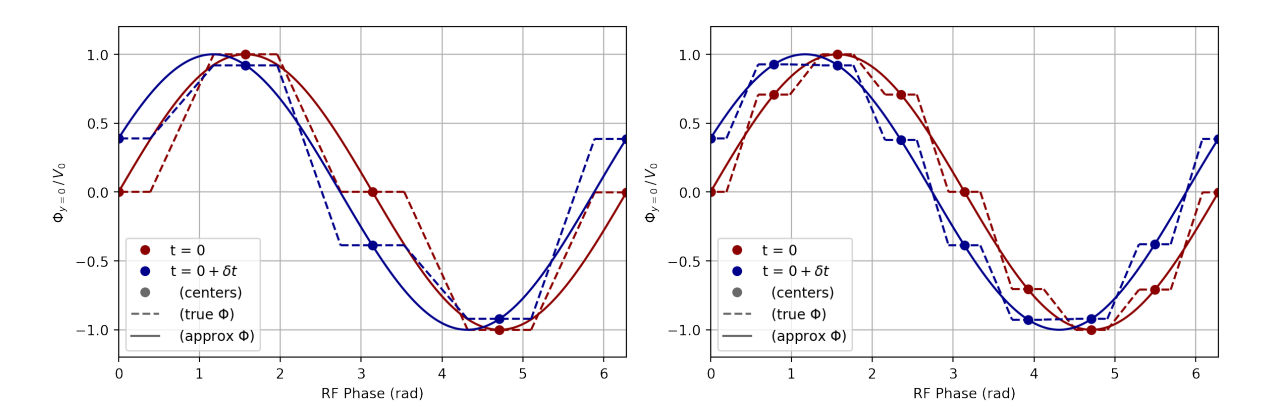


Figure 2: Smooth potential approximation along carpet surface for a four-phase array (left) and eight-phase array (right)

Having developed the appropriate suite of analytic techniques we proceed to delineate the required operating parameters of RF carpets for barium collection in high pressure xenon gas. Section 6 discusses the problem in general terms, and briefly outlines application specifications in terms of geometry, coverage, power and pressure. In Sec. 7 we establish the key RF carpet operating parameters for high pressure xenon gas environments, paying careful attention to the details of ion transport microphysics in this environment. Sec. 8 presents our main result, an assessment of the required carpet parameters for transport barium ions in high pressure xenon gas neutrinoless double beta decay experiments. Sec. 9 presents our conclusions, which are that existing carpet structures based on precision printed circuit boards (PCBs) [9] appear viable at pressures up to one bar, whereas 10 bar operation for the neutrinoless double beta decay application exceeds the capabilities of such structures. The required operating parameters for use at 10 bar may potentially be accessible with devices based on micro-fabrication techniques used for micro-electromechanical systems and trapped ion quantum information science applications [32, 33, 34] and large wafer CMOS processes. We briefly discuss the near-term R&D needed to realize such devices.

139

140

141

143

147

152

155

156

157

159

2. Dynamics of ion levitation and transport on phased RF carpets: analytic treatment

A purely N-phased RF carpet powered by a peak-to-peak RF voltage of V_{pp} is one with voltage V_j on the jth electrode at time t of:

$$V_j(t) = \frac{V_{pp}}{2} \sin\left(\Omega t + \frac{2\pi j}{N}\right). \tag{1}$$

For the purposes of our calculations we make the approximation that this generates a smooth potential along the carpet surface of the form:

$$\Phi(x,y,t)|_{y=0} = \frac{V_{pp}}{2}\sin\left(\Omega t + \frac{2\pi}{Np}x\right). \tag{2}$$

We choose a coordinate system such that the RF electrodes are strips running along the z direction. The direction x runs radially along the carpet in the direction ions will be transported, with y perpendicular to the carpet with y=0 defining the carpet surface. This geometry also well approximates a local region of a circular carpet, in the case where the electrode ring radii are significantly larger than the strip-to-strip spacing. This approximation neglects the finite width of the electrodes and the flat potential across them, as shown in Fig. 2. The approximation becomes increasingly precise for larger the values of N, and we will explore its limitations quantitatively in Sec. 3. Using the potential Eq. 2 as a boundary condition for Laplace's equation the electric potential over all space can be obtained:

$$\Phi_0(x, y, t) = \frac{V_{pp}}{2} \sin\left(\Omega t + \frac{2\pi}{Np} x\right) \exp\left(-\frac{2\pi}{Np} y\right),\tag{3}$$

from which the driving electric field can be found. It is of a fixed magnitude at every position, rotating at constant angular velocity:

$$\vec{E}(\vec{r},t) = \frac{V_{pp}}{2} \frac{2\pi}{Np} \exp\left(-\frac{2\pi}{Np}y\right) \vec{u} \left[\Omega t + \frac{2\pi}{Np}x\right], \qquad \vec{u}(\theta) = \begin{pmatrix} \cos(\theta) \\ -\sin(\theta) \\ 0 \end{pmatrix}. \tag{4}$$

Notably this is not of Dehmelt form typical in a Paul trap, which would require an electric field like 162 $E(x,t) = E(x)e^{i\Omega t}$; nevertheless, we will see similar trapping dynamics in the vertical direction emerge. 163 We seek solutions to the following driven equation of motion, where the ion moves in response to both 164 the applied RF voltages and a superimposed DC push field E_{push} toward the carpet, with mobility μ :

$$m\ddot{\vec{r}} + \frac{q}{\mu}\dot{\vec{r}} = q\left[\vec{E}(\vec{r},t) - E_{push}\hat{y}\right]. \tag{5}$$

As is conventional with treatment of radio-frequency trap systems we make an assumption that the trajectory $\vec{r}(t)$ can be factorized into a micro-motion $\xi(t)$ and macro-motion $\vec{z}(t)$: 167

$$\vec{r}(t) = \vec{z}(t) + \vec{\xi}(t), \tag{6}$$

where the dynamics of $\vec{\xi}$ are determined by the RF frequency and the dynamics of \vec{z} are slower and emergent. Unlike the simple Dehmelt-like trap, in this system the relevant frequency of the micro-motion is not exactly Ω , because the ion is moving laterally while passing through the RF field. It is convenient 170 to introduce ion co-moving coordinates as $\vec{x} = \vec{r} - \langle \vec{v}(y) \rangle t$ where $\langle \vec{v}(y) \rangle$ is the mean ion velocity at fixed 171 height y; in these coordinates we find that

$$\vec{E}(x,t) = \frac{V_{pp}}{2} \frac{2\pi}{Np} \exp\left(-\frac{2\pi}{Np}y\right) \vec{u} \left[\tilde{\Omega}(y)t\right], \qquad \tilde{\Omega}(y) = \left(\Omega + \frac{2\pi}{Np}\langle \vec{v}(y)\rangle\right). \tag{7}$$

For transverse trajectories at fixed $\langle \vec{v} \rangle$, the ion will experience an electric field which is rotating spatially at 173 frequency Ω , and this is thus the frequency of the micro-motion. We will need to solve for $\langle \vec{v} \rangle$ generated by this micro-motion, which is also required to predict $\tilde{\Omega}$ and thus the trajectory mean height, in an iterative manner. Substitution of the electric field into the equation of motion and neglecting the slow-varying derivatives of macro-coordinates yields an equation of motion for the micro-motion:

$$m\ddot{\vec{\xi}} + \frac{q}{\mu}\dot{\vec{\xi}} = q\frac{V_{pp}}{2}\frac{2\pi}{Np}\exp\left(-\frac{2\pi}{Np}y\right)\begin{pmatrix} \cos\tilde{\Omega}t\\ -\sin\tilde{\Omega}t\\ 0 \end{pmatrix},\tag{8}$$

with y being the y-component of the macro-coordinate \vec{z} . Eq. 8 can be solved for $\vec{\xi}(t)$:

174

175

177

$$\vec{\xi}(t) = -\chi \, \vec{u}[\tilde{\Omega}t - \eta], \qquad \chi = \frac{q}{m\tilde{\Omega}\sqrt{D^2 + \tilde{\Omega}^2}} \frac{V_{pp}}{2} \frac{2\pi}{Np} \exp\left(-\frac{2\pi}{Np}y\right). \tag{9}$$

The micro-motion executes circles of radius χ around the smoothly moving $\vec{z}(t)$ macro-trajectory. We 179 have introduced the constant D associated with damping of the ballistic ion motion by gas collisions and the phase factor η which dictates by how much the micro-motion phase trails the E-field direction: 181

$$D = \frac{q}{\mu m}$$
, and $\eta = \arctan\left[-D/\tilde{\Omega}\right]$. (10)

The relationship between the directions of $\vec{\xi}(t)$ and $\vec{E}(t)$ are illustrated in Fig 3, left. To solve for the 182 macro-motion, we insert Eq. 6 into Eq. 5, the equation of motion, and average over one full micro-cycle. 183 We find the governing equation for the macro-motion $\vec{z}(t)$:

$$m\langle \vec{z}\rangle_{\tilde{\Omega}} + \frac{q}{\mu}\langle \dot{z}\rangle_{\tilde{\Omega}} = q\langle \left(\vec{\xi}.\vec{\nabla}\right)\vec{E}[\vec{z}]\rangle_{\tilde{\Omega}} - qE_{push}\hat{y},\tag{11}$$

into which we can substitute $\vec{\xi}$ from Eq. 8 and extract the effective force driving $\vec{z}(t)$ emerging from the 185 micro-motion: 186

$$F_{i} = -\frac{q^{2}}{m\tilde{\Omega}\sqrt{D^{2} + \tilde{\Omega}^{2}}} \langle \nabla_{j}E_{i}[\vec{z}]R_{jk}[-\eta]E_{k}\rangle_{\tilde{\Omega}}, \tag{12}$$

following methods analogous to those outlined in the Appendix. Here $R_{ik}[\theta]$ is a rotation matrix in the xy plane by angle θ . Evaluating this effective force explicitly:

$$\vec{F} = \frac{q^2}{m\tilde{\Omega}\sqrt{\left(D^2 + \tilde{\Omega}^2\right)}} \left(\frac{2\pi}{Np}\right)^3 \left(\frac{V_{pp}}{2}\right)^2 \exp\left(-\frac{4\pi}{Np}y\right) \left(\begin{array}{c} \sin\left(\eta\right) \\ \cos\left(\eta\right) \end{array}\right). \tag{13}$$

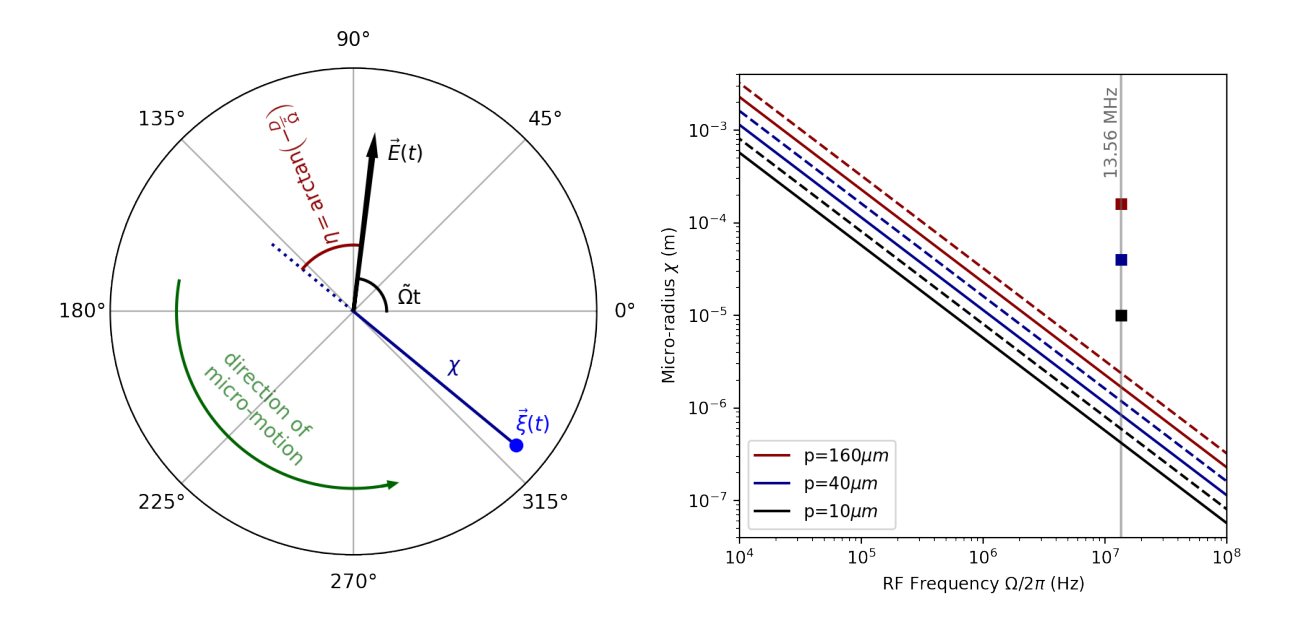


Figure 3: Left: Polar plot showing relationship between E-field direction and micro-motion vector in terms of damping constant D and effective local frequency $\tilde{\Omega}$. Right: Comparison of predicted micro-radius for N=2 (solid) and N=4 (dashed) lines for $E_{push}=20~{\rm V~cm^{-1}}$ and m=952 amu (a representative cluster mass of a barium dication in xenon gas at 10 bar) vs. frequency. For the operating parameter point considered later in this work (Ω =13.56 MHz) the micro-radius is always much smaller than the carpet pitch (shown as square markers).

Note that $\eta=0$ is the fully ballistic case; in this scenario we find a force which acts only in y to repel the ion from the carpet. On the other hand as η becomes larger a force pushing the ion along the carpet also appears. Once the motion becomes completely viscous, the force levitating the ion above the carpet disappears entirely. Dependence of the phase η upon the relative contributions of ballistic vs. damped dynamics thus dictates the extent to which the micro-motion conspires with the electric field to provide a levitating force.

The ion transverse velocity $\langle v_x \rangle$ at height y can be found by considering the transverse component of the 2D equation of motion, averaged over a micro-cycle. In terms of the x-component of the effective force F_x :

$$\langle v_x \rangle = \frac{\mu}{q} F_x = \frac{\mu q}{m \tilde{\Omega} \sqrt{\left(D^2 + \tilde{\Omega}^2\right)}} \left(\frac{2\pi}{Np}\right)^3 \left(\frac{V_{pp}}{2}\right)^2 \exp\left(-\frac{4\pi}{Np}y\right) \sin\left(\eta\right) \tag{14}$$

$$= \frac{Dq\mu}{m\tilde{\Omega}\left(D^2 + \tilde{\Omega}^2\right)} \left(\frac{2\pi}{Np}\right)^3 \left(\frac{V_{pp}}{2}\right)^2 \exp\left(-\frac{4\pi}{Np}y\right). \tag{15}$$

The final equality requires application of trigonometric identity to obtain $\sin [\eta] = -\frac{D}{\sqrt{D^2 + \Omega^2}}$. If we assume that $\delta = \frac{2\pi \langle \vec{v} \rangle}{Np\Omega}$ is a small parameter so that it is appropriate to use Ω rather than $\tilde{\Omega}$ in the expression for v, we find the leading order approximation:

$$v \sim v_0 = \frac{Dq\mu}{m\Omega \left(D^2 + \Omega^2\right)} \left(\frac{2\pi}{Np}\right)^3 \left(\frac{V_{pp}}{2}\right)^2 \exp\left(-\frac{4\pi}{Np}y\right). \tag{16}$$

In any situation where this approximation is insufficient, it is possible to proceed iteratively to calculate higher order corrections to \vec{v} if necessary. For example, the first order correction to $\langle \vec{v} \rangle$ can be found by substituting $\langle \vec{v} \rangle_0$ into $\tilde{\Omega}$ in Eq. 15 and expanding to first order in δ :

$$v = v_0 \left[1 - \frac{2\pi}{Np\Omega} \frac{D^2 + 3\Omega^2}{D^2 + \Omega^2} + \dots \right].$$
 (17)

We will not generally need these higher order terms in this work, the leading order expression being accurate with only percent-level corrections. This completes the treatment of the macro-dynamics in the horizontal direction. In the vertical direction, the ion will be acted on by two competing forces, the

repulsive force generated by the micro-motion and the attractive force generated by the push field. These two forces balance when

$$qE_{push} - \frac{q^2}{m\tilde{\Omega}\sqrt{\left(D^2 + \tilde{\Omega}^2\right)}} \left(\frac{2\pi}{Np}\right)^3 \left(\frac{V_{pp}}{2}\right)^2 \exp\left(-\frac{4\pi}{Np}y\right) \cos\left(\eta\right) = 0.$$
 (18)

We can thus consider the ion as being trapped within a Dehmelt-like pseudo-potential of the form

$$V = \frac{q}{m\left(D^2 + \tilde{\Omega}^2\right)^2} \frac{1}{2} \left(\frac{2\pi}{Np}\right)^2 \left(\frac{V_{pp}}{2}\right)^2 \exp\left(-\frac{4\pi}{Np}y\right) + E_{push}y. \tag{19}$$

Where once again we have employed a useful trigonometric identity yielding $\cos [\eta] = \frac{\Omega}{\sqrt{D^2 + \Omega^2}}$. The pseudo-potential has a minimum at height $\langle y \rangle$ given by

$$\langle y \rangle = \frac{Np}{4\pi} \ln \left[\frac{2qV_{pp}^2}{m\left(D^2 + \tilde{\Omega}^2\right)E_{push}} \left(\frac{\pi}{Np}\right)^3 \right], \tag{20}$$

which is the height at which the ion levitates above the carpet for stable transverse motion. The radius of the micro-motion at this height has an especially simple form, which is independent of both ion mobility and RF driving voltage,

$$\chi(\langle y \rangle) = \sqrt{\frac{Np}{2\pi} \frac{qE_{push}}{m\tilde{\Omega}^2}},\tag{21}$$

For a stable trajectory to exist, we must enforce $\chi \ll \langle y \rangle$, otherwise the micro-trajectory will intercept the carpet surface during its motion. Fig. 3, right shows the calculated micro-radii for the parameter points considered later in this work, and shows that the micro-radii at the driving frequency of interest will always be small relative to the carpet pitch, and much smaller than the hence stable trajectory height. The micro-radius need not be considered further in what follows.

218

219

220

222

224

225

227

228

234

236

237

238

The transverse velocity of the ion at this height also has an especially simple form, and is to leading order:

$$\langle v_x \rangle = \mu E_{push} \frac{D}{\Omega}. \tag{22}$$

The effective vertical trap depth in electronvolts can be found by simply evaluating $V(\langle y \rangle) - V(0)$. The trap depth has dependencies on all of N, p, μ, m, q, V_{pp} and E_{push} via Eq. 19, and further exploration follows in later sections.

3. Finite electrode width effects beyond the leading order geometrical approximation

In the calculations of the two-phase RF carpet performed by Schwarz [7], the Dehmelt potential is calculated accounting for the effects of finite electrode width and assuming linear voltage drop across the intermediate insulator. The calculations for the phased arrays presented above neglect these effects and assume a sinusoidal profile over the carpet surface. This approximation is expected to become increasingly good as N becomes large. We can gain an estimate of the magnitude of these effects for the worst case N=2 by comparing the effective Dehmelt potential from Schwarz with that for an equivalent N=2 phased array treated under our approximation scheme. In both cases, the expression for the pseudo-potential in the y direction reduces to the form:

$$V_{N=2}(y) = E_{push}y + X \frac{1}{\tilde{\Omega}^2 + D^2} \frac{q}{m} \left(\frac{V_{pp}}{p}\right)^2 \exp(-2\pi y/p).$$
 (23)

The pre-factor X depends on which calculation is used. For the Schwartz-like calculation with gap-to-pitch ratio of 0.5, we find $X = \frac{8}{\pi^2}$, and for gap-to-pitch ratio of 0 it is X = 1. For our N-phase calculation with N = 2 which assumes a sinusoidal surface potential (realized approximately but not exactly for all gap-to-pitch ratios), we obtain $X = \frac{\pi^2}{8}$. Since the effective levitating force is proportional to V_{pp}^2 , taking these three results as an ensemble we can conclude that the detailed structure of the electrodes for a given pitch maps to an uncertainty on the required RF voltage of around $\pm 8.5\%$, loosely estimated as the standard deviation of the three approximation schemes.

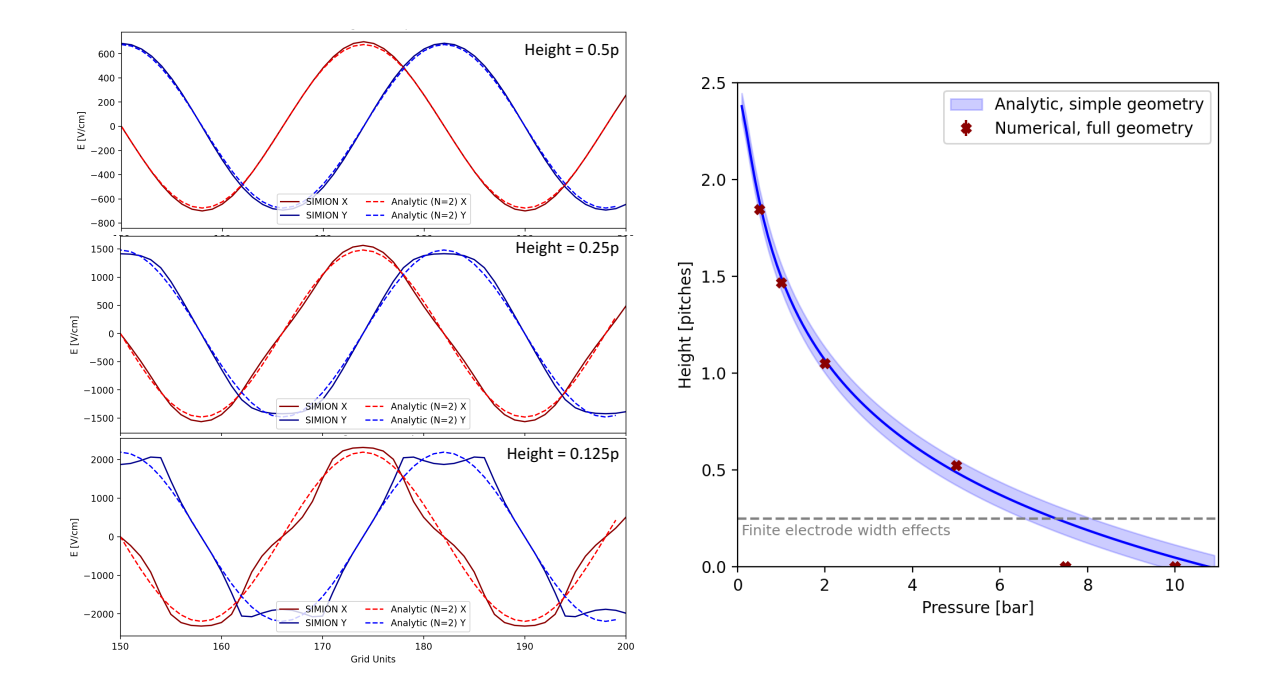


Figure 4: Finite electrode width effects on RF carpet transport. Left: comparison of idealized calculation of electric fields to full numerical simulation of RF carpet geometry, evaluating both X and Y field components at various heights from the carpet surface. Effects due to finite electrode widths only become manifest below around 0.25 pitches from the surface, above which they quickly decay away. Right: Comparison of stable trajectory heights in the idealized analytic calculation and full numerical simulation of ions through the calculated E fields. At surface-to-ion distances below around 0.25 pitches the higher order field terms cause ions to crash into the carpet surface. This calculation is evaluated as m=136 amu, $\mu_0=39.9~{\rm cm}^2{\rm V}^{-1}{\rm s}^{-1}$, $E_{push}=20~{\rm V~cm}^{-1}$, $V_{pp}=300~{\rm V}$, N=4, corresponding approximately to the conditions of barium ion transport in helium.

Inclusion of higher Fourier mode terms associated with the potential surface, which may be associated with either finite-width electrodes or at sub-leading level with surface imperfections, leads to another important effect: the appearance of near-field effects at short distances from the carpet, which can destabilize the micro-motion from circular orbits. These higher order terms will be determined by the precise voltage structure on the carpet boundary, and take the form in 3D space dictated by Laplace's equation:

242

243

244

246

247

250

253

254

255

257

261

262

263

$$\Phi(x,y,t) = \sum_{a} \Phi_{a}(x,y,t), \qquad \Phi_{a}(x,y,t) = \left[A_{a}(t) \sin\left(a\frac{2\pi}{Np}x\right) + B_{a}(t) \cos\left(a\frac{2\pi}{Np}x\right) \right] \exp\left(-\frac{2\pi}{Np}ay\right). \tag{24}$$

We see from this expression how terms with a > 1 decay away from the surface more quickly than the leading a=1 sinusoidal term, which is why the first order approximation is effective for describing dynamics of the field at relatively large y. We can obtain an estimate of the magnitude of the effects of these higher order terms by comparing the idealized calculation of ion motion with a numerical simulation in the full geometry, absent stochastic effects. An RF carpet geometry with $160 \,\mu\mathrm{m}$ pitch was implemented within the SIMION software package and simulated in four-phase mode. Comparison of the leadingorder field configuration against the full finite-element simulated field map from SIMION is shown at various surface-to-ion heights in Fig. 4 left. We observe that already by around 0.25 electrode pitches p above the surface, the effects of the higher-order terms become vanishingly small within the precision of the calculation. Simulating ion trajectories through this numerically derived field configuration with stochastic fluctuations disabled shows an excellent agreement with the analytic expression at all surfaceto-ion distances above $0.25 \times p$; below this distance, ions begin to crash into the carpet due to higher order perturbations to their micro-motion. Fig. 4, right, shows this comparison for a toy system with ion mass 136 amu moving with mobility $\mu = 39.9~\mathrm{cm^2~V^{-1}~s^{-1}}$, $E_{push} = 20~\mathrm{V~cm^{-1}}$ and $V_{pp} = 300~\mathrm{V~RF}$ voltage (the approximate conditions for barium ion drift in helium buffer gas at 1 bar) as a function of pressure over an N=4 carpet.⁴ The blue band in Fig. 4 represents the $\pm 8.5\%$ RF voltage uncertainty described

 $^{^4}$ We note that to obtain this precision, SIMION had to be operated with increased E field refine convergence of 0.0005 and

above, and has a small effect. For any stable trajectory localized more the $0.25 \times p$ from the surface, we conclude that finite electrode width effects are negligible in determining the dynamics of phased RF carpets, whereas below $y_{loss} = 0.25 \times p$ they generate near-field effects that cause ions to crash into the surface. The surface at $y_{loss} = 0.25 \times p$ can thus be considered as being an effective surface-of-noreturn for transverse ion transport due to near-field effects. The continued relevance of this surface in the presence of stochastic effects will be an assumption of the thermodynamic model developed in later sections.

4. Stochastic effects from Brownian motion and the equivalence of the thermodynamic model

The calculations of Sec. 2 do not capture the important effects of stochastic perturbations to the trajectory caused by Brownian collisions with gas atoms or molecules. These effects are especially critical for understanding the dynamics of systems where the ion mass is large and the motion relatively viscous, as in our systems of interest. These perturbations are the dominant cause of ion losses from the trapping region in high pressure gases.

There are multiple approaches to the problem of simulating buffer gas interactions with varying degrees of reliability. Within SIMION, two simulation methods are widely used. An approximate "statistical diffusion simulation" (SDS) [14, 35] method applies random impulses to the numerically evaluated trajectory to simulate the integrated effect of many random interactions with the buffer gas. The SDS model is expected to be valid in scenarios where ions travel in straight lines between collisions. Since inter-collision curvature is the hallmark of RF carpet operation that allows for ion levitation, validity of the SDS model for our purposes appears questionable. Similar conclusions have been reached by other authors, regarding use of the SDS model at radio frequencies and high pressures [31, 36, 37]. A second approach involves micro-physically simulating the trajectory collision-by-collision with hard-sphere interactions [38]. This is more accurate but is far more computationally expensive. Here we undertake simulations using the hard sphere model and show that the effects of micro-physically simulated stochastic perturbations can be well described using a novel thermodynamic and kinetic formalism using the concept of thermalization into the pseudo-potential, allowing for much more rapid evaluation of the viable parameter space.

Figure 5, left shows a microphysical simulation within the hard sphere model, using ion mass m=952 amu (for reasons to be explained in Sec 7), push field $E_{push}=80~{\rm V~cm^{-1}}$, buffer gas M=136 amu, collision cross section $\sigma=6\times10^{-19}~{\rm m^2}$, pressure = 1 bar, RF frequency $\Omega=13.56~{\rm MHz}$, RF voltage $V_{pp}=700~{\rm V}$, carpet pitch $p=40~{\rm \mu m}$. This somewhat artificial simulation parameter point was picked to show a regime where both the stochastic deviations of the trajectory and the micro-motion are visible within a single simulated trajectory. In cases where one distance scale dwarfs the other, illustrating the dynamics of the motion in a single image is more challenging. The ion is placed high above the carpet and initially travels directly downward with the push field. It then experiences a transition to an RF carpet transport trajectory once the ion is near enough the carpet to be significantly influenced by the RF forces. We observe the characteristic spiral motion of the micro-trajectory which causes levitation superposed on a random walk motion and a tendency to move from left to right, in the direction of the traveling RF wave phase. Eventually in this geometry the ion reaches the end of powered part of the carpet and is driven down to the surface by the push field near R=0.

To compare calculations with stochastic effects from the hard sphere model to analytic models, we must have a full suite of parameters for calculation of the pseudo-potential and the quantities that derive from it. In most cases this is straightforward, though under hard sphere dynamics the mobility of the ion is an emergent property rather than an input parameter. Kinetic theory can be used to obtain a prediction for this quantity in terms of the hard sphere model parameters,

$$\mu = \frac{3q}{16n} \sqrt{\frac{2\pi}{\mathcal{M}kT}} \frac{1}{\Omega_M}.$$
 (25)

Where \mathcal{M} is the reduced mass, n is the gas number density and Ω_M is the momentum transfer cross section, which for $m \gg M$ is equivalent to the geometrical cross section for hard-sphere collisions. In

enhanced tracking quality T.Qual>20, above which precision the solution converged. Running with previously recommended settings E field refine conference 0.005 and tracking quality T.Qual=0 lead to artificially strong performance levitation of ions at short distances.

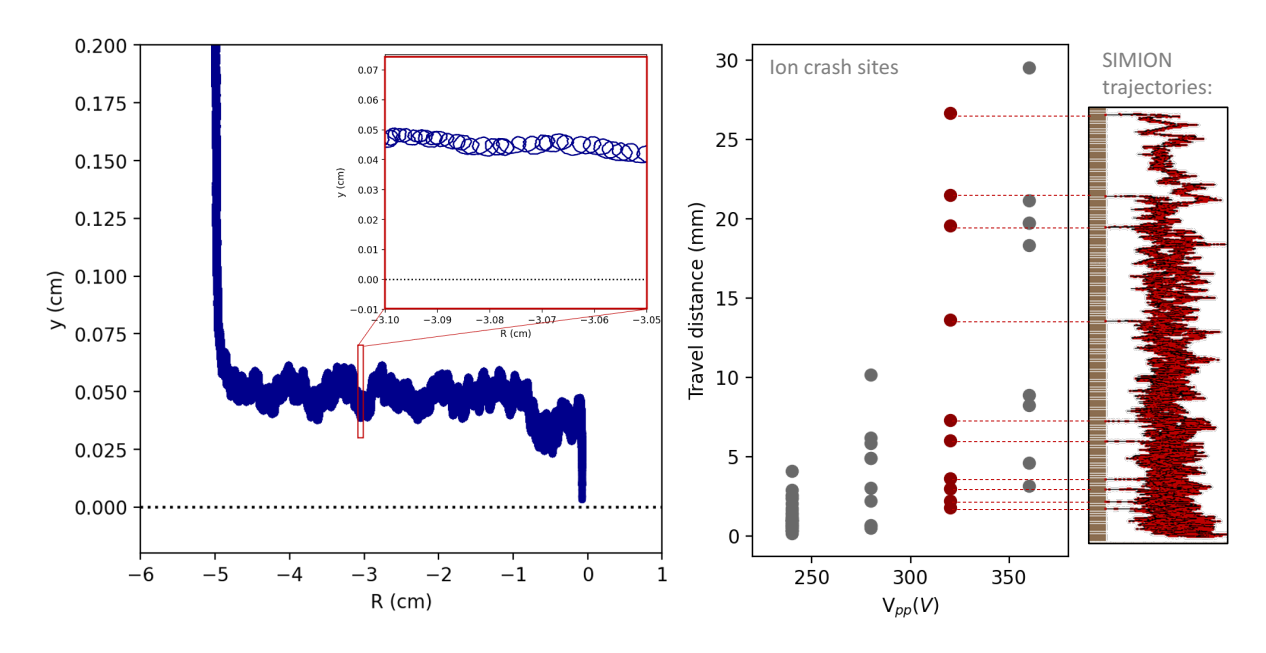


Figure 5: Left: Phased RF carpet simulation showing dynamics of micro-and macro-motion for a successfully transported ion trajectory. Right: examples of SIMION-simulated trajectories experiencing losses into the RF carpet surface; Right: travel distance for ensembles of 10 ions at various RF driving voltages which begin at z=0. The full SIMION trajectories for the 320 V data points are shown to the right for illustration. In this sub-figure, x runs vertically and y horizontally, with ion crash sites mapped to the middle scatter plot.

terms of our input parameters:

$$\mathcal{M} = \frac{mM}{m+M}, \qquad n = n_0 \frac{P}{P_0}, \qquad \Omega_M = \pi (2R_{Xe})^2.$$
 (26)

For the purposes of this demonstration we take R_{Xe} to be the Van Der Waals radius of xenon, $R_{Xe} = 216 \,\mathrm{pm}$ yielding $\Omega_M = 6 \times 10^{-19} \,\mathrm{m}^2$. We will take this prediction for the mobility to complete the information needed to compare the microphysical simulation with the analytic prediction. Agreement between the mobility emerging from SIMION with hard-sphere collisions and kinetic theory was validated using drift simulations in DC fields to be better than 5%, with precision limited only by fluctuations in the simulated trajectories.

When stochastic effects are incorporated, the distribution of ion heights above the carpet is no longer tightly bunched around the stable macro-trajectory, but distributed around it by thermal motion. Since ions in dense gases remain to a good approximation in thermal equilibrium, we can consider the following conjecture: the ions undergoing collisions with the Maxwellian distributed buffer gas should distribute with a Boltzmann spectrum within the pseudo-potential, in the local rest frame of the gas. This conjecture is non-trivial, since the pseudo-potential treatment technically only applies to ions following equilibrium trajectories, and only in one dimension of 3D space in this system. If the thermalization conjecture is indeed satisfied, we would expect the vertical height distribution of ions undergoing stochastic collisions with buffer gas above the carpet to take the form:

$$\rho_{Therm}(y) = \frac{\exp\left[-qV(y)/k_BT\right]}{\int_0^\infty dy' \exp\left[-qV(y')/k_BT\right]}.$$
(27)

Figure 6 shows the comparison of the height distribution projected from the thermalization conjecture with the distribution predicted by detailed microphysical simulations for two carpet configurations, one with three-phase RF driven at $V_{pp}=400$ V and one with four-phase RF driven at $V_{pp}=700$ V. These two simulations have parameters informed by the application of interest (m=952 amu, M=136 amu, $p=160\,\mu m,\,P=1$ bar, T=273 K) but are shown for illustrative purposes only; precise calculations that properly include the pressure-dependent mobility and ion mass will be given in later sections. The thermalization conjecture is satisfied to a good degree of approximation in both cases, despite different operational parameters. In simulation scans over many conditions undertaken during this work we have observed strong agreement with the thermalization conjecture in all cases. The small deviations from the precise form of the distribution function observed in Fig. 6 are expected due to the finite transport distances simulated.

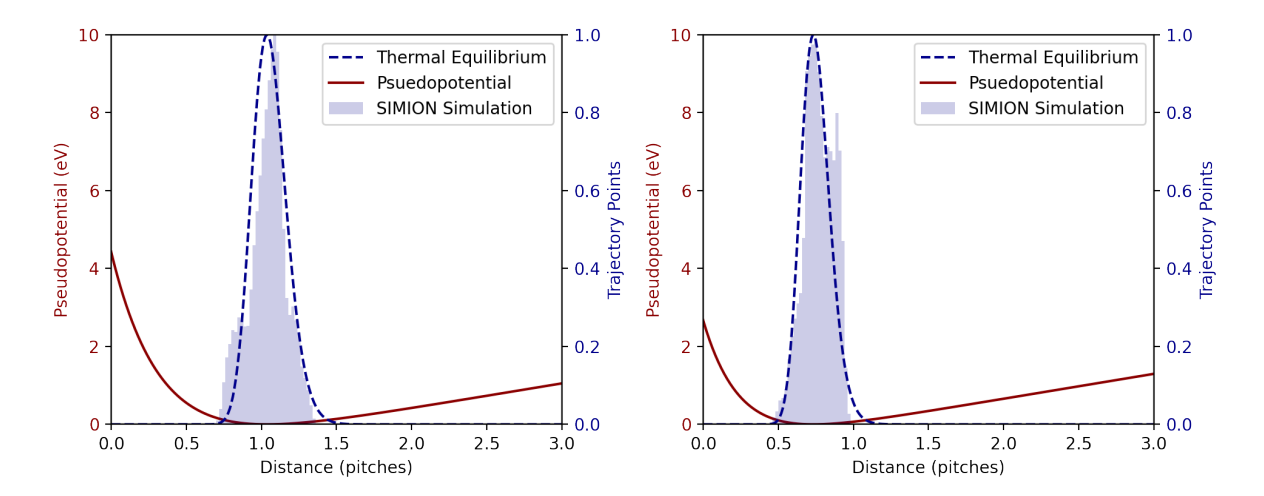


Figure 6: Demonstration of the validity of the thermalization conjecture for (left) N=4, $V_{pp}=700V$ and (right) N=3, $V_{pp}=400V$. The other operating parameters are m=952 amu, M=136 amu, $p=160\,\mu m$, P=1 bar, T=273 K.

The full simulation of ion trajectories, accounting for every collision in dense gases, is an expensive and inefficient computational prospect. The validity of the thermalization conjecture, however, allows us to explore more rapidly the space of possibilities for stable RF carpet operation at a given pressure and electric field configuration. What we ideally wish to know is not only the ion height distribution, but whether ions can travel for large distances along the carpet surface without losses.

First, we note that it is obvious that when there is no stable trajectory, or $\langle y \rangle < 0$, all ions will be quickly lost onto the carpet surface. Rearranging this condition we can find a minimal value of V_{pp} for transport to be plausible,

$$V_{pp} \ge \sqrt{\frac{m\left(D^2 + \tilde{\Omega}^2\right)E_{push}}{2q}\left(\frac{Np}{\pi}\right)^3}.$$
 (28)

Above this driving RF voltage, stable transport is possible because the pseudo-potential well is deepest at some position above the carpet rather than below it. However, there will still be losses due to stochastic effects at finite buffer gas densities: no matter how strong the effective repulsive force, the equilibrium distribution will have some small tail that runs below the surface height. These losses are manifest as ion crashes after random distances, with the mean distance depending on the applied RF voltage. Fig. 5, right shows an example set of simulations at various RF voltages using the conditions described above with the random crashes at various distances illustrated.

Ion losses are substantial when the equilibrium probability distribution of ion heights has a substantial contribution at or below the surface beyond which ions are lost, established in Sec. 3 to be around $y_{Loss} = 0.25 \times p$. Thus the condition for long-lived ion levitation can be expressed as

$$\phi = \frac{\int_{-\infty}^{y_{Loss}} dy \, \rho_{Therm}(y)}{\int_{-\infty}^{\infty} dy' \, \rho_{Therm}(y')} \ll 1. \tag{29}$$

While qualitatively interesting for understanding the conditions for stability, this argument is not very useful in practice, since it is unclear how we should interpret \ll quantitatively. The ion loss rate depends not only on the thermal distribution, but also on how fast ions explore that distribution. To obtain an estimate for the theoretical ion loss rate for the potential we must consider ion kinetics as well as thermodynamics.

For simplicity of exposition in the following we assume ions to be lost at the surface y=0, though in practice we will set this value equal to y_{Loss} for predicting ion loss rates in the calculations that follow. At sufficiently high pressures we can consider that the trapped ions are undergoing constant collisions with the buffer gas, maintaining thermal equilibrium. To a good approximation each scattering interaction causes the ion to obtain a random velocity in a random direction, sampled from the Maxwell-Boltzmann distribution. Consider now the motion of an ion between two collisions separated by mean collision time T. To hit the wall following such a collision an ion at position y must have a velocity of at least $v_y = y/T$ in the y direction. Thus between these two collisions the probability for ion loss is

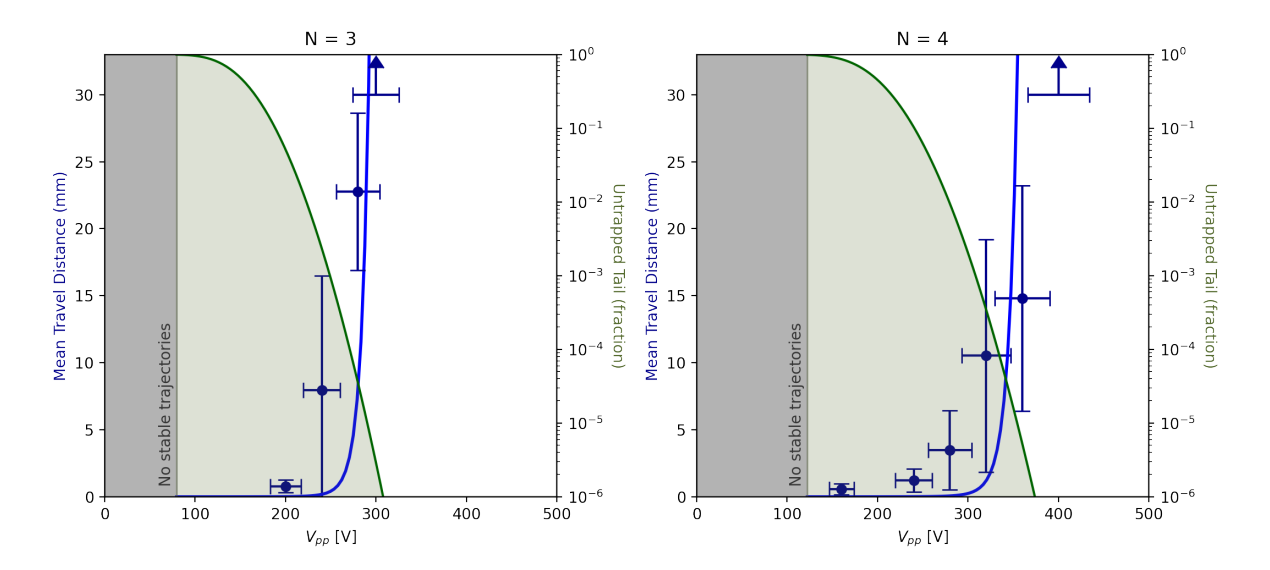


Figure 7: Comparison of simulated and theoretical ion survival distances for N=3 and N=4 phased arrays at 160 μm pitch, m=952 amu, M=136 amu, $p=160\,\mu m$, P=1 bar, T=273 K. The grey shaded area represents the region where $\langle y \rangle < 0$ so no stable trajectories exist. The green curve shows the integral of the negative tail of the thermal distribution below $y_{Loss}=0.25\times p$, to be read using the right logarithmic axis. The blue line shows the predicted mean ion survival distance, assuming validity of the thermodynamic arguments of this paper. The blue data points show the results of a detailed, collision-by-collision simulation in the SIMION software package. The error bars show mean and standard deviation over a sample of an ensemble of simulated ions. Strong qualitative agreement between the theoretical model and the microscopic simulation is observed, in particular in specifying the location of the sharp transition from lossy to relatively lossless transport.

$$\mathcal{P}(T) = \int_{-\infty}^{0} dv_y f(v) \int_{0}^{v_y T} dy \, \rho(y). \tag{30}$$

If the collision time is short, as will always be the case in high density buffer gases, we can approximate that $\rho(y) = \rho(0)$ everywhere the above integral has support. Thus the probability for an ion loss between these two collisions can be evaluated as

$$\mathcal{P}(T) = \langle v_n^- \rangle T \rho(0). \tag{31}$$

In this expression, $\langle v_y^- \rangle$ is the mean negative velocity in the y direction, which can be evaluated from Maxwell-Boltzmann statistics,

$$\langle v_{-} \rangle = \int_{-\infty}^{0} dv \, v \sqrt{\frac{m}{2\pi kT}} \exp\left(-\frac{mv^2}{2kT}\right) = \sqrt{\frac{kT}{2\pi m}}.$$
 (32)

Finally we can calculate the expected loss rate per unit time Γ_t and per unit distance along the carpet Γ_d respectively:

$$\Gamma_t = \frac{1}{T} \mathcal{P}(T) = \sqrt{\frac{kT}{2\pi m}} \rho(0), \qquad \Gamma_d = \frac{1}{\langle v_x \rangle} \Gamma_t.$$
 (33)

Thus we obtain statistical predictions of ion loss rates in distance and time, based on the previously demonstrated thermalization conjecture augmented with kinetic arguments. Figure 7 shows the comparison of simulated ion loss rates from a complete collision-by-collision SIMION simulation to the thermodynamic prediction, for similar operating parameters to atmospheric pressure xenon gas operation. Quantitative agreement is observed. In particular, while the ion survival distances in the transition region are highly variable, the sharp transition from stable to unstable transport around a certain well-predicted critical voltage is reproduced in both the analytic model and simulation.

5. Comparative analysis of N-phased array performance characteristics

377

378

379

381

384

385

In the previous sections we have proven that the important properties of phased RF carpet ion transport, including stochastic effects from ion-gas interactions leading to ion losses into the carpet, can be modeled analytically and without computationally expensive simulation ensembles.

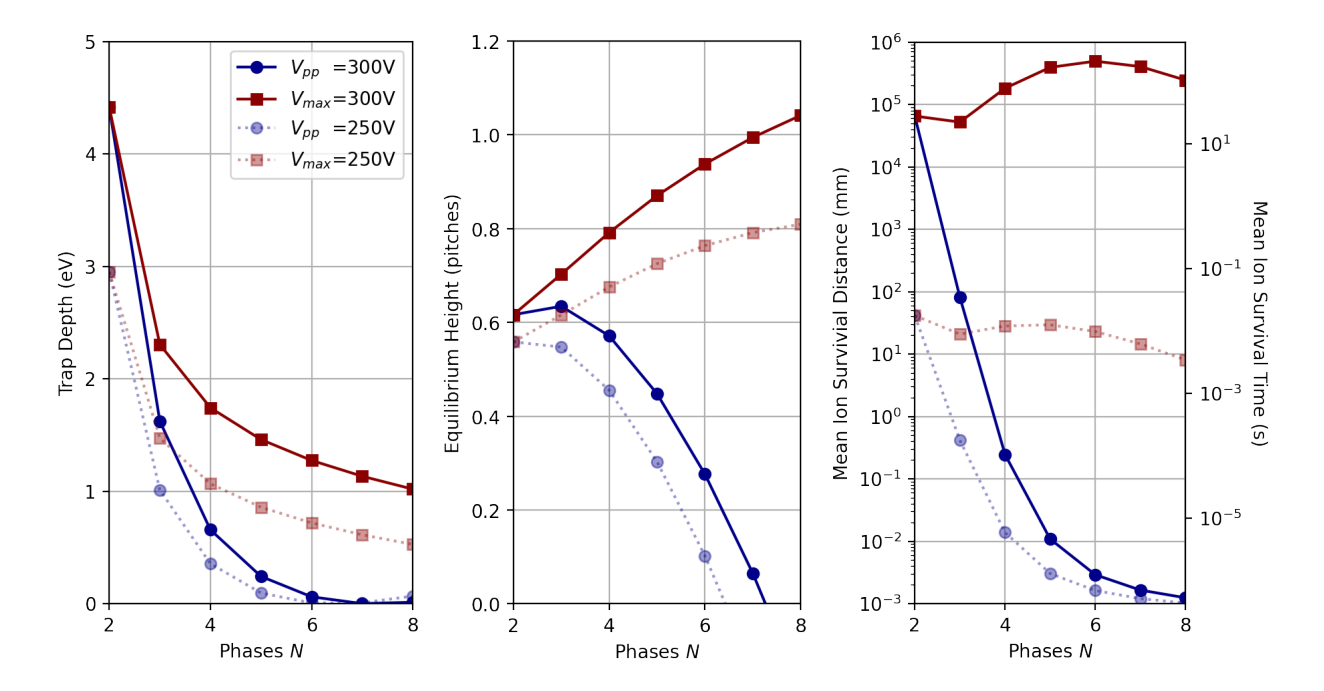


Figure 8: Dependence of RF carpet stability parameters on phasing N for a 160 μ m carpet. The left plot shows trap depth in eV, center shows equilibrium ion transport height (the minimum of the pseudo-potential) and the right plot shows the mean survival distance and lifetime, calculated according to the thermodynamic protocol outlined in this paper. The operating parameters are m = 952 amu, M = 136 amu, $p = 160 \mu m$, P = 1 bar, T = 273 K.

In this section we demonstrate why phase orders $N \geq 3$ may be considered compelling relative to the simpler N=2 system, already discussed by Schwarz [7]. As shown in the left two panels of Fig. 8 (blue lines), for the same fixed RF driving voltage V_{pp} , trap depth and equilibrium ion height both will generally fall with N. This naturally implies a reduced mean ion survival distance, as shown in Fig. 8, right (blue lines), which would seem to imply N=2 as an optimum operating phase structure. Since the mean transport velocity Eq. 22 does not depend on N or V_{pp} we label this figure with both mean survival time and survival distance axes, though with the caveat that the N=2 data point should technically only be interpreted according to the mean survival time metric, since in this case Eq. 22 is inapplicable given no tendency to drive the ion in one direction or the other.

The highest voltage that can be applied to an RF carpet is limited by breakdown, either through the buffer gas or through the carpet insulating material. In an N-phased system, the maximal voltage between any adjacent pair of electrodes scales as:

$$V_{max} = V_{pp} \sin\left(\frac{\pi}{N}\right). \tag{34}$$

which is less than V_{pp} for a $N \geq 2$ phased system (see Fig. 11). This relationship can be inverted to provide a maximal allowed drive voltage for an N-phase carpet limited by material dielectric strengths. The higher driving voltages that can be applied to $N \geq 2$ phased arrays then compensate for some of the performance degradation introduced by reducing the levitating field gradients. This is shown in Fig. 8 (red lines). While the trap depth continues to drop with increasing N for fixed V_{max} , the equilibrium ion height above the carpet increases; this countervailing effect leads to a non-trivial dependence of mean survival distance on N, as shown in Fig. 8, right. For an operating voltage of 300 V and a pitch of 160 μ m, the optimal array phasing appears closer to N=6. Practical issues such as arranging for supply of N distinct RF phases to one small-pitch carpet structure or power dissipation considerations may favor smaller N than this optimal choice, but from the point of view of ion transport dynamics alone, intermediate values for the carpet phasing are preferable, contrasting to some degree our conventional intuition.

412 6. Application of phased RF carpets for neutrinoless double beta decay

For a ton-scale high pressure xenon gas detector operating at 10 bar, similar to the system⁵ described in Ref. [39], barium ions will naturally drift in the applied electric field to the cathode plane, which is likely to be of order 2 m in diameter. RF carpets have been demonstrated to efficiently transport ions over similar distance scales [40]. However, the highest operating pressure investigated to date has been 300 mbar. RF carpets for use at higher gas pressures would require much smaller pitches and higher applied RF voltages than have been previously demonstrated. Nevertheless, several arguments suggest that such an application is not entirely unfeasible:

- 1. High pressure xenon gas has a breakdown voltage dramatically in excess of helium, so larger RF operating voltages can be employed. This enhancement was tested experimentally in Ref. [41], which ultimately proved that dielectric materials such as kapton will likely break down before the gas in the detector at spacings relevant for RF carpet operation.
- 2. Molecular ion formation around dications in xenon gas is expected to enhance their mass for the purposes of transport at high pressure. This physics was elaborated and a detailed theoretical presented in Ref. [17]. This effect is especially strong for doubly charged ions, leading to an important stabilization effect in RF transport.
- 3. Technologies to produce large RF carpets at somewhat smaller pitches than the present state of the art appear viable, employing nano-fabrication methods. Scaling to large radii is a manufacturing challenge, but not an obviously insurmountable one.

The choice to study an N-phased carpet (Fig. 1, c) in this work is motivated by practicality for the TPC application. A more traditional two-phase + transverse DC field approach (Fig. 1, a) appears unviable, since it would either imply non-axial electric fields within the detector, or else a strongly varying push field across the RF carpet if placed behind a gating grid. An RF wall+surfing approach (Fig. 1, b) may be viable, but theoretical evaluation is prohibitive given the trajectories in such a system are not analytically calculable. It may nevertheless be possible to prove such systems fit for purpose in this regime empirically.

While detailed design of a barium tagging phase of of xenon gas double beta decay program remains both speculative and outside the scope of the present work, it is possible to consider a set of plausible requirements for an RF carpet array used as part of a barium tagging sub-system. A sketch of one possible implementation is shown in Fig. 9.

A single RF carpet of 2 m radius is not required for a barium tagging cathode, as long as ions arriving anywhere on the cathode surface are captured and transported to a sensor. Several practical requirements on the RF carpet system are eased both by modularizing the barium sensing system into sub-units and employing electrostatic focusing to the extent possible. In the scheme of Fig. 9, ions first drift to the cathode where they are guided by static fields to an array of RF several carpets, each concentrating ions to one single molecule fluorescent imaging ion sensor. A full coverage of the \sim 2 m diameter cathode with seven RF carpet sub-units, with electrostatic focusing by a factor of four in field strength implies the need for seven 30 cm diameter RF carpets, which would demand efficient ion transport for at least 15 cm of distance. Stronger electrostatic focusing may in principle be viable before the TPC operation becomes unstable, though with some active gas volume sacrificed for the focusing volume.

The required drift field of a time projection chamber is larger than the small $E_{push} \sim 20 \text{ V cm}^{-1}$ required for RF carpet operation to be efficient, even without electrostatic focussing. Thus the ions must necessarily travel from a high-field region of the TPC into a low-field region of the RF carpet volume. In an electrostatic system this would imply losses of ions on whatever gate structure separates these regions. In an electrodynamic mode, however, ion losses through this transition can be averted by timed gating. In an electroluminescent time projection chamber the projected arrival time of an ion at the carpet plane can be straightforwardly established online by comparing the time difference between primary (S1) and secondary (S2) scintillation signals generated by the much faster drifting electrons. These signals are both acquired by the energy detection system, which is a mandatory component of any neutrinoless double beta decay time projection chamber experiment. Upon arrival of the ion within the RF carpet sweep region, the local electric field can be switched from the high value required for efficient drift to the lower value required for a stable push-field. This switch can be applied at trigger level, without detailed online event reconstructions, for all events within a broad energy energy region of interest based on uncalibrated

⁵Ref. [39] proposes 15 bar operation. The same detector system could, however, be operated at 10 bar, which we have chosen as the benchmark pressure for this work to match the operating pressure of existing NEXT detector phases.

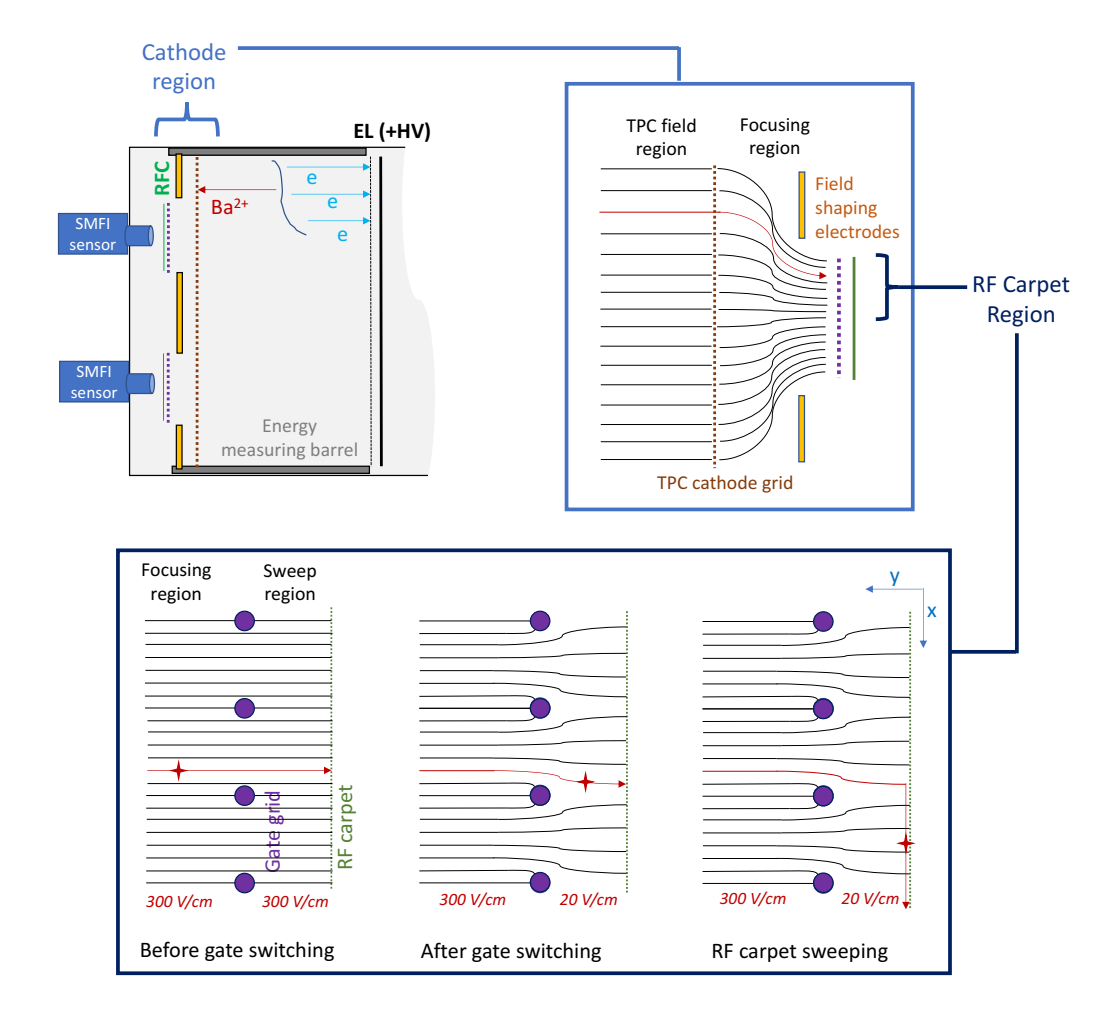


Figure 9: Sketch of a possible RF carpet implementation for a xenon gas double beta decay search. Thin black lines show a cartoon of the electric field lines (though concentration and expansion factors of the fields will likely be much larger than indicated here). The top left figure shows an outline of the cathode and its relation to other parts of the detector. Electrons drift rapidly to the anode where they produce electroluminescence light in O(1) ms after the event, whereas ions drift to the cathode in O(1) second where they are captured in the RF carpet sweep region by a switching gate grid.

S2 pulses. Neither the voltage difference (\pm a few hundred volts) nor the required speed (\sim 1 ms) or timing precision (\sim 0.1 ms) of this switch appear to be prohibitive, and it does not interfere with the electric field in the detector drift region, which remains stable, although temporarily insensitive to barium ions.

There are many conceivable arrangements of the RF carpet system geometry, with varying details of coverage, shape, and segmentation. One factor that is likely to strongly influence the choice of geometry is power consumption, which must be managed with care. For carpets with the fine pitches that will be considered for our application of interest, resistive losses are the dominant source of power consumption over dielectric ones. The power lost to resistive heating depends on the radius as well as the pitch and connectivity of RF electrodes. The power dissipated in a single, fully connected 2 m diameter, μ m pitch carpet operated at 1000 V and 1 MHz is likely to be unviably large (potentially at the 1 MW level, though with significant dependencies on choice of both insulator and conductor materials). Dividing the carpet into smaller sub-units and reducing their surface coverage can reduce this power consumption considerably. Resistive heating of a fully connected RF carpet scales with approximately the forth power of the radius, with both the total capacitance and total length of conductor factoring into the heat load. The modularized scheme as described therefore implies a significantly reduced power consumption relative to a single fully carpeted cathode surface, estimated to be of order 4 kW for the set of seven fully connected, 30 cm diameter RF carpets. Azimuthally segmenting the ring electrodes into six segments per carpet could further reduce the resistive heating for the same coverage to around 100 W by reducing the lengths of each conductor that must be charged and discharged. While it is beyond the scope of this work to attempt a detailed optimization of system geometry, or to present detailed power-draw calculations, it is recognized that power consumption is likely to be a relevant consideration for a final design in addition to those presented here, likely managed primarily through system geometry optimization. System considerations may also limit the deployable number of RF phases.

Finally we note that, since establishing coincidence between a detected double beta decay event and the collected barium ion is mandatory for barium tagging, transport speed along the carpet surface is also a relevant performance parameter. Given the low rate of events expected with energy near Q_{bb} , a time delay from landing to arriving at a sensor of 10 seconds can be easily accommodated. All efficient transport scenarios we explore will meet this requirement comfortably, so ion delivery speed is not a considerable design driver.

7. System parameters for RF carpets in high pressure xenon gas

Following the previous sections of general discussion we now turn attention to the RF carpet operating parameters that may be appropriate for barium ion transport in high pressure xenon gas. These inputs to this calculation can be divided into two categories. First, the input parameters associated with the medium or ion, which are fixed by nature and we cannot change; second, the input parameters we may adjust by choice of technology or operating conditions.

7.1. Gas and ion parameters

The following parameters are considered intrinsic properties of the system, and will not be adjusted during this study.

Gas composition / atomic mass M: The gas in a high pressure xenon gas neutrinoless double beta decay experiment can be assumed to be predominantly 136 Xe with an atomic mass of 136. Possible addition of minority components to reduce diffusion or absorb neutrons, such as 4 He [42, 43, 44, 45] or 3 He [46] respectively may also be present. Unlike electrons, ions are always thermalized at the drift fields of interest, and so a minority component of a light noble gas will not impact either the instantaneous energy spectrum or bulk mobility of drifting ions, and we can assume m=136 amu for the mass of the buffer gas with a reasonable expectation of accuracy for all these cases. Incorporation of a molecular gas such as CH_4 [47] or CH_4 [48, 49, 50, 51] and others such as CO_2 [52] and CH_4 [53] have also been proposed, though this requires more involved filtering schemes to purify the working gas mixture to the part-per-billion levels of purity in oxygen and water required for TPC operation. Incorporation of such a molecular species would lead to non-trivial chemistry forming molecular ions with the drifting barium cluster, and so we do not consider it here.

Ion charge q: Barium ions produced in any double beta decay event are created in a very highly charged state as emerging electrons disrupt the decaying atom. Within picoseconds these highly charged initial ions have captured electrons from surrounding neutral xenon atoms until this capture process

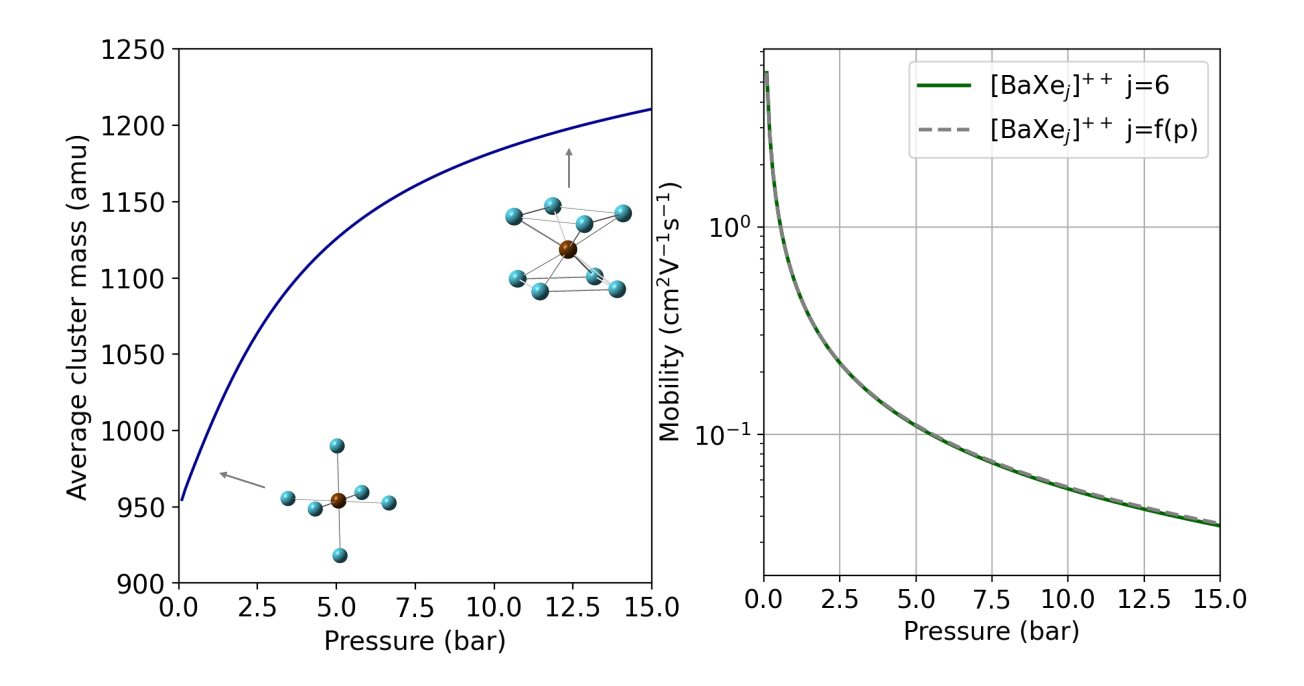


Figure 10: Left: mean cluster mass vs. pressure using methods of Ref [17]. Right: mobility vs. pressure from Ref [17]. The pressure dependencies of these parameters have important implications for the pressure dependence of RF carpet operation in the pressure range 1-10 bar.

becomes energetically disfavored, a process which terminates at Ba²⁺. In high density environments such as in liquid or solid xenon, recombination of thermalized charge near the ion leads to further neutralization, leading to a distribution of barium charge states. In xenon gas at densities up to at least 50 bar, recombination is expected to be minimal, as illustrated in Refs. [54] and [55], and so the ions can be assumed to be in the pure 2+ charge state.

Ion mass m: The mass of the bare daughter ion 136 Ba is 136 amu. This ion has a high charge density and xenon atoms are easily polarizable, and thus the ion quickly becomes dressed with a shell of neutral xenon atoms. Calculations of molecular ion formation in the $\mathrm{Ba^+/Xe}$ system using density functional theory [17] agree very well with experimental data which show a strongly pressure dependent reduced mobility, the hallmark of molecular ion formation [18]. In the $\mathrm{Ba^{2+}/Xe}$ system, similar calculations predict formation of significantly larger clusters, with a mean Xenon binding number of 6–9 depending on gas pressure. The binding energies are 3–4 eV, far above thermal energies, suggesting these clusters should be thermally stable as they are driven by the RF carpet. The lightest cluster predicted has m=952 amu, and this was used as a reference parameter point in the earlier sections in this paper for this reason. In this calculations that follow we use the predicted pressure-dependent mean cluster mass extracted from the simulation results of Ref. [17], shown in Fig. 10, left. In general, both the trap depths and mean ion travel heights improve for larger values of m so the expected molecular ion formation can be considered as a beneficial effect for RF carpet operation in high pressure xenon.

Ion mobility μ : In Ref. [17], potential energy surfaces evaluated with density functional theory were used to calculate the momentum transfer cross section between neutral xenon atoms and the expected ion clusters in high pressure xenon gas. These cross sections were then used to obtain the ion mobility. In the case of the Ba⁺/Xe system, the relative mass of the average cluster changes dramatically with pressure in the 0.1–10 bar range, since the mass of bare barium and [BaXe]⁺ are very different, and this substantially influences the reduced mobility as a function of pressure. However, for the Ba²⁺/Xe system the relative mass of the cluster is less dependent on pressure and hence the reduced mobility varies less drastically. Fig. 10, right shows the predicted mobility, either assuming a fixed cluster size of 6 (dashed grey line) or accounting for the predicted pressure-dependent scaling of cluster size (green line). The difference between these predictions is small, with absolute mobility scaling with a fairly constant reduced mobility μ_0 as $\mu = \mu_0 \frac{p_0}{p}$. This pressure dependence of absolute mobility leads to increased damping at high pressures, however, and can be understood as one of the fundamental reasons why RF carpets become more challenging to use at high operating pressures.

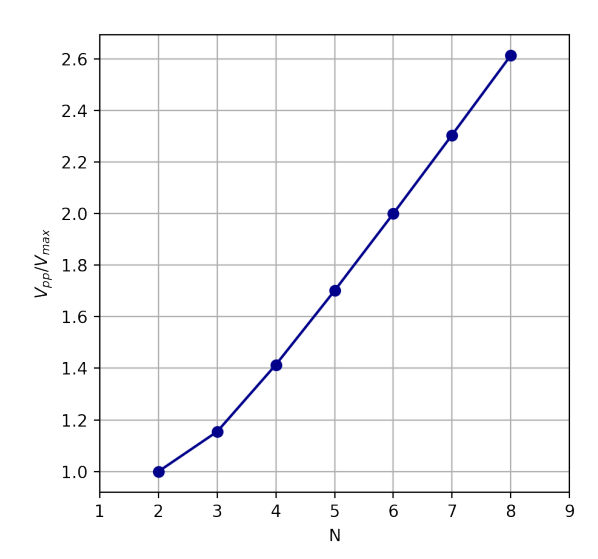


Figure 11: Dependence of maximal electrode-to-electrode voltage V_{max} with carpet phasing N for a fixed peak-to-peak voltage V_{pp}

7.2. RF carpet parameters and their constraints

The following parameters are adjustable based on design choices, and our goal in this work is to establish the values that would allow for stable transport in barium tagging applications:

Pitch p: The RF carpet pitch defines the distance between two electrode centers. The smaller the pitch, the stronger the levitating effect of the RF carpet. Present large RF carpet manufacturing techniques aiming for fine pitches have used a single layer PCB etch on Kapton substrate with pitches of around 160 μ m [9]. State-of-the-art PCB manufacture is capable of still smaller pitches, down to 25 μ m trace and gap width [56], yielding 50 μ m pitch. Manufacturing methods for RF structures used in ion traps for quantum information processing have, however, achieved far finer feature sizes than 50 μ m [32, 57, 58, 33, 59] and manufacture by photo-etch on sapphire or by CMOS production both appear possible for achieving feature sizes as small as 5μ m [34]. RF carpets of this scale have been proposed, but not yet demonstrated, by others [31]. Ongoing R&D within the NEXT collaboration aims to produce an RF carpet by single-layer photo-etch on sapphire of pitch of $15\mu m$ for experimental studies of ion transport in xenon gas.

Carpet phasing N: In principle any phasing is possible, though the complexity of supplying the various RF voltages to independently biased groups of traces becomes more difficult as the phasing gets larger. N=2 phasing is the simplest option, though this does not allow for transverse motion without also applying either a DC sweep field or a surfing wave. A DC sweep field is not ideal for use in a NEXT detector since it would require one carpet edge to be highly biased relative to the ion collection point, under which conditions it would be challenging to maintain a sufficiently small push field across the array without a rather complex gating geometry. The study of Sec. 5 showed N=3 gave particularly poor performance. We thus pick N=4 as our benchmark. Calculations for N=5 and N=6 show minimal improvement in the transport efficiency for small pitches, certainly insufficient to justify the additional complexity associated with a 5 or 6 phase RF structure.

RF peak-to-peak voltage V_{pp} : The RF peak-to-peak voltage is limited by the breakdown voltage for discharges over the carpet surface or through the insulating material(s), at some threshold voltage V_{max} , as described in Sec. 5 and shown in Fig. 11. For the N=4 carpets that will be used as example cases in the following sections, the ratio of V_{max} to V_{pp} is around 1.4. Generally speaking, breakdown through the buffer gas has limited operating voltage of all previous RF carpets. Typically in helium gas it is possible to reach applied voltages around $V_{pp}=150$ V. Xenon gas has a far higher breakdown strength than helium gas, and elevated pressures increase this breakdown voltage still further. Past measurements of the breakdown of thin Kapton layers at RF frequencies in xenon gas suggest that in high pressure xenon gas experiments, breakdown of insulator substrate will be limiting before breakdown through the gas for kapton PCBs operated at gas pressures above 1 bar. Data from Ref. [41] showed breakdown

occurring through kapton films at approximately $V_{max} = 500 \text{ V}$ for 130 μ m insulator distance, though it is likely that in a practical RF carpet this value may be somewhat higher due to the higher quality of the electrode surfaces. Several commercially available kapton films advertise a dielectric strength as high as 8 kV for a 25 μ m film thickness, suggesting that with suitably well-prepared electrodes, much larger voltages may be supportable on kapton substrates [60]. Additionally, experience in the ion trapping community with micro-fabricated traps has shown that insulating structures with feature sizes on the scale of 10 μ m can satisfactorily withstand $V_{max} = 1000 \text{ V}$, for example, Ref. [32]. We thus speculate that kapton-based PCB carpets probably cannot safely hold voltages much above 500 V RF at $\mathcal{O}(50 \,\mu\text{m})$ pitch sizes, whereas nano-fabrication methods have been demonstrated which allow up to 1000 V over 10 μ m spacings, in principle.

RF frequency Ω : In our calculations we have considered fixed RF frequencies of 13.56 MHz due to easy availability of RF generators at this frequency for industrial application in plasma production [61], though in principle, carpet operation at any RF driving frequency is conceivable. In the heavily damped regime all quantitative results concerning stability are nearly independent of RF frequency in realistic ranges, so we do not scan over this parameter. Since RF carpet power consumption is minimized by choosing the lowest frequency possible, it is likely that such a system would be operated at the lowest driving frequency where stable operation can be achieved. For the small pitches considered here this is around 1 MHz, below which the micro-radius will become comparable to the equilibrium ion height, leading to trajectories which are no longer well represented by macro-motion within the pseudo-potential well.

Push field E_{push} : The push field is what drives ions toward the carpet and, counteracting the RF levitating force, creates the trapping effect. Normal operation of a time projection chamber using high pressure xenon gas would naturally create a perpendicular field into the cathode of order $E_{push} = 300$ V cm⁻¹. This is too large for stable RF carpet transport under reasonable operating conditions, since typical push fields in RF carpet systems are often of the order 10–30 V cm⁻¹. As discussed in Sec. 6, this mis-match invokes the need for a gating grid which switches when ions arrive. Using the scheme described earlier, a push field of 20 V cm⁻¹ can be applied to allow for efficient ion transport.

Temperature T: All the NEXT detectors to date have operated at room temperature, $T \sim 293$ K. Reduced temperature operation of future phases has been considered in order to reduce the dark noise present in silicon photo-multipliers to levels that may allow them to be used for energy measurement in addition to tracking, and to relieve mechanical constraints on the system by offering higher densities at lower pressures. Reducing the operating temperature of the detector will cause ions in the pseudo-potential to thermalize at a lower temperature, narrowing their distribution around the stable trajectory and leading to enhanced stability. This is expected to offer a modest enhancement to RF carpet efficiency, since the mean cluster sizes and ion mobilities are also temperature dependent. Xenon freezes at around 219K at 10 bar, and so certainly the system cannot be operated below this temperature. In what follows we will evaluate transport distances at both room temperature and at T = 220 K to illustrate the (relatively modest) effects of temperature changes.

8. Operating conditions for RF carpets in high pressure xenon gas

We now apply the methods of the previous sections to the question of ion transport efficiency in xenon gas at atmospheric pressure and above. We begin by considering operation of RF carpets in xenon at 1 bar, which appears likely to be achievable with existing technical solutions using kapton-based PCBs. Fig. 12 shows the calculated pseudo-potential for various pitches and RF voltages given a push field of E_{push} =20 V cm⁻¹ and RF frequency of 13.56 MHz in one bar of xenon gas. Potentials for both singly and doubly charged barium ions are shown, and all calculations include the effects of clustering on both mobility and molecular ion mass. At 80 μ m pitch and 1 bar pressure, stable transport requires a voltage near to but not in excess of the edge of viability for kapton substrates. As expected, reducing the carpet pitch leads to dramatic improvement in the depth and vertical position of the pseudo-potential well.

As the pressure is raised, stable transport becomes increasingly challenging. Fig. 13 shows pseudo-potential curves as well as calculated thermal probability distributions at room temperature for several RF carpet pitches and RF voltages at 10 bar. Consideration of the probability distributions shown in the lower panel of this figure illustrates that stable transport cannot be expected at 10 bar for carpet pitches above a few tens of microns, or electrode-to-electrode voltages below 700–800V. At operating points with lower voltages or larger pitches, the ion height probability distributions clearly have large tails penetrating the carpet surface, implying rapid ion losses.

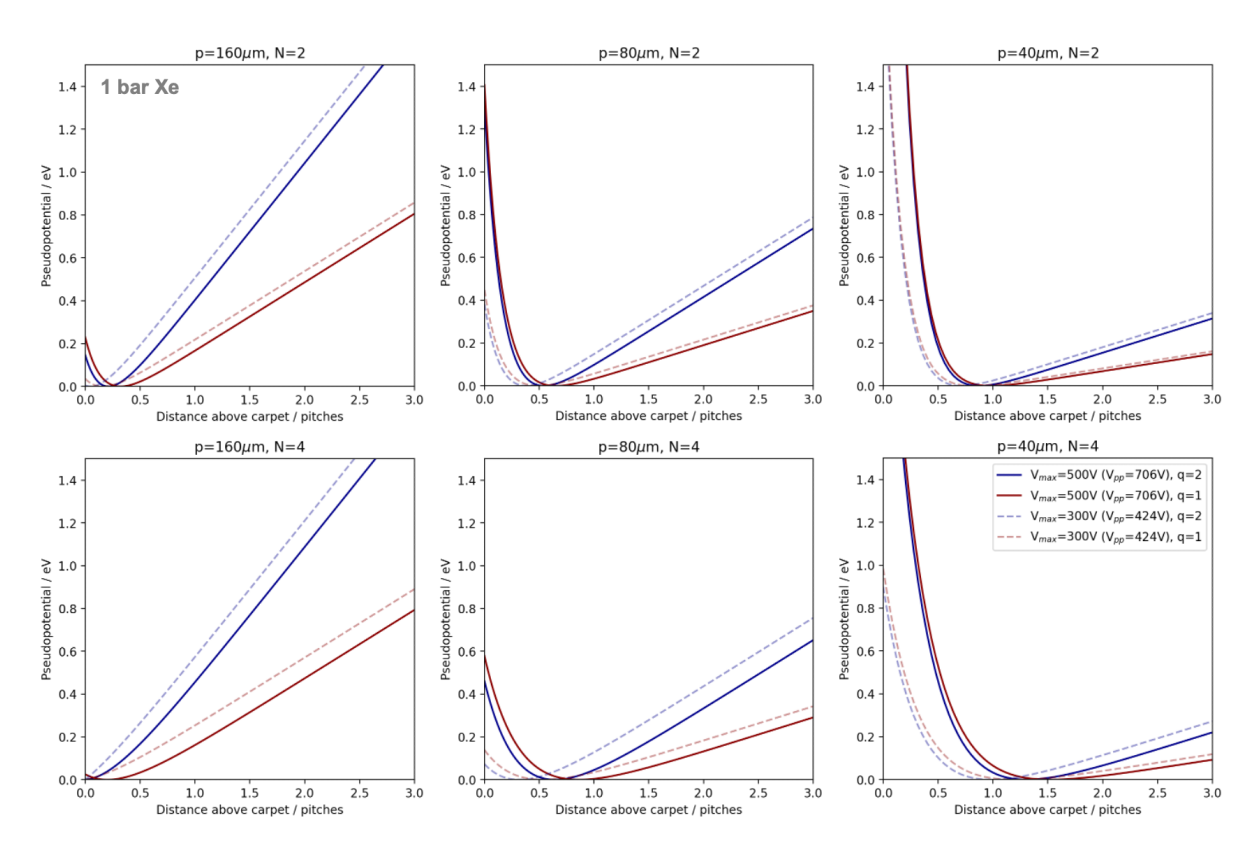


Figure 12: Pseudo-potential wells calculated for one bar xenon gas for singly and doubly charged barium ions at room temperature. Stable trapping is clearly possible for Ba^{2+} in all but the least favorable scenarios.

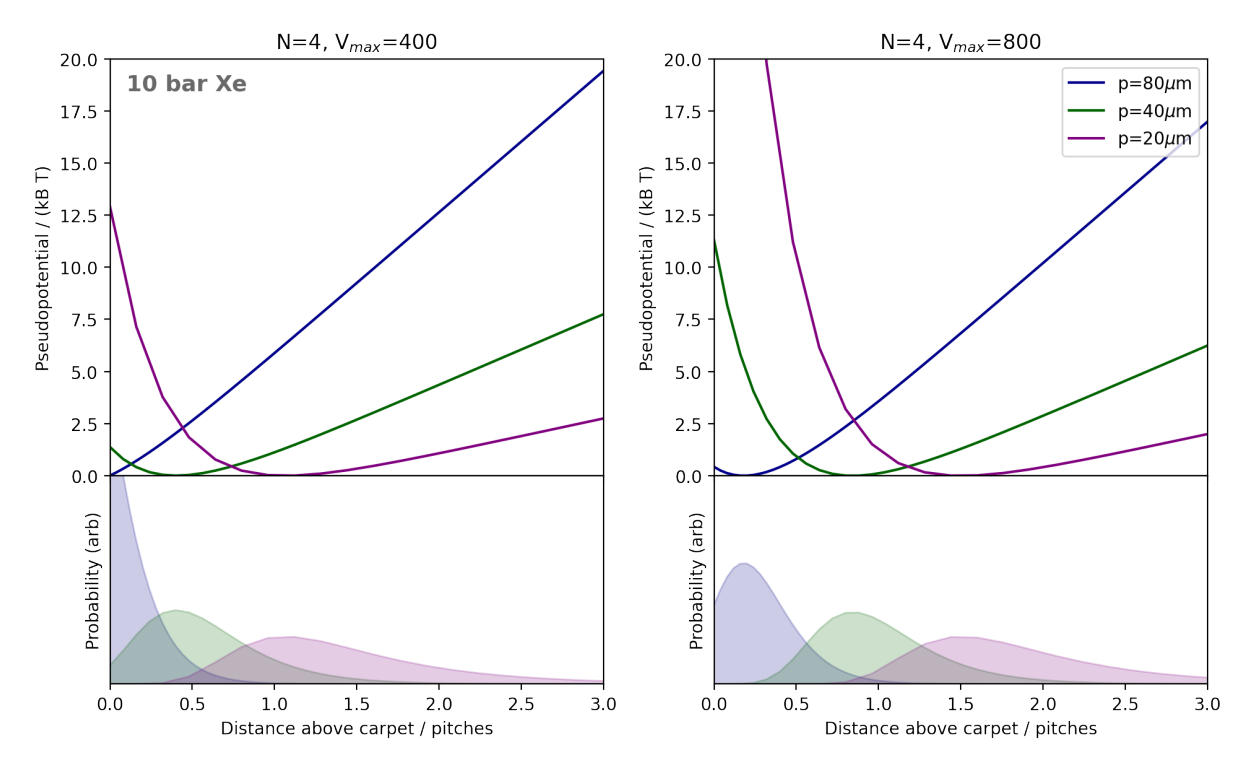


Figure 13: Examples of potential curves and ion height thermal probability distributions in 10 bar xenon gas for $\mathrm{Ba^{2+}}$ within its xenon cluster with N=4 RF carpets. The three colored curves show three different pitches achievable with nanofabrication methods; the two figures show two different RF driving voltages. In the upper panel we show the pseudo-potential in units of $k_B T$ and in the lower, the equilibrium ion height distribution.

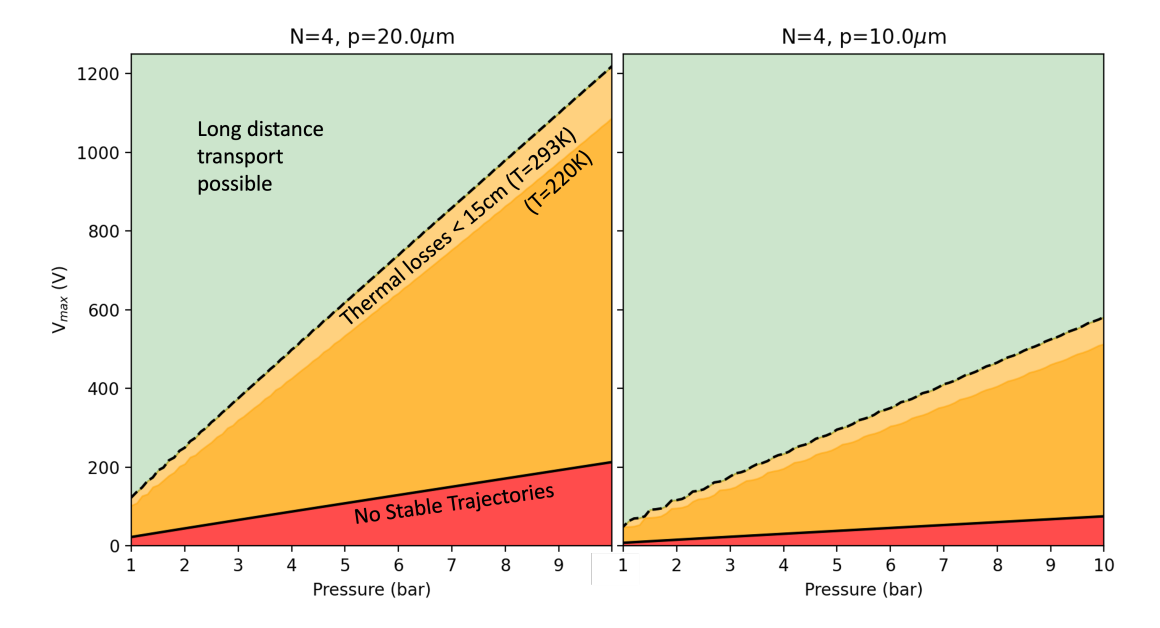


Figure 14: RF carpet stability regimes with fixed pitch and variable pressure. In the red region, the minimum of the psuedo-potential is not above the carpet surface. In the yellow regions, ions travel less than 30 cm on average at the two tested temperatures. The green region covers the parameter values where ions travel more than 30 cm on average at 293 K. Due to the rapid threshold-like form of the transport efficiency, the regions for 50 cm average travel are only different by a few percent in RF voltage.

The figure of merit that is the ultimate determinant of viability for RF carpets for ion transport in xenon gas detectors is the mean transverse ion survival distance. We define as our requirement here as at least 15 cm predicted transport distance, though it is clear from the curves of, for example, Fig. 7 that once the threshold for stable transport is crossed, mean travel distances climb extremely rapidly with voltage. The difference in operating voltage required for a mean distance of 15 cm or 50 cm is thus only at the few percent level. To establish the possible parameter space of RF carpet operation we first fix the operating pitch, pressure, push field, frequency, ion charge, mobility and temperature. We then calculate the curve of mean survival distance vs. RF voltage using the methods of Sec. 4. Finally we interpolate this curve to evaluate the voltage threshold where 15 cm mean transport distance is achieved. This will be considered as the threshold voltage for efficient transport at this operating parameter point.

Results of scans in pressure at fixed pitch are shown in Fig. 14, and complementary scans in pitch at fixed pressure are reported in Fig. 15. These figures are the main quantitative results of this work, encoding the operating requirements for RF carpets for high pressure xenon gas. Also shown on the figure is the region where even absent thermal fluctuations, no stable ion trajectories exist. The large disparity between this region and the stable long-distance transport regime highlights how vital the incorporation of finite temperature / stochastic effects is to predicting the stability of RF carpet operation, in contrast to much less strongly damped vacuum-based trap systems.

9. Discussion and Conclusions

In this paper we have explored the theoretical operating conditions for N-phased radio-frequency carpets in high pressure gases. The micro and macro-motion of ions on phased RF arrays has been derived via generalization of the Dehmelt potential formalism, with analytic expressions obtained for all important transport parameters. In high pressure environments, the analytic solution for the macro-motion is modified by stochastic fluctuations due to buffer gas interaction. Diffusion of the particle trajectory from the minimum of the pseudo-potential into the carpet surface due to Brownian motion is the dominant mechanism of ion loss in high buffer gas densities, and thus a proper understanding of this deviation is required for understanding transport efficiency of RF carpets in dense gases. Detailed collision-by-collision simulations in SIMION were used to validate a new model for RF carpet performance based on thermodynamics and kinetic theory, which are used to accurately describe both the equilibrium ion height distribution and the mean ion loss rate, respectively. The validity of this model alleviates the need for computationally expensive simulations, which become untenable for high operating pressures and long transport distances.

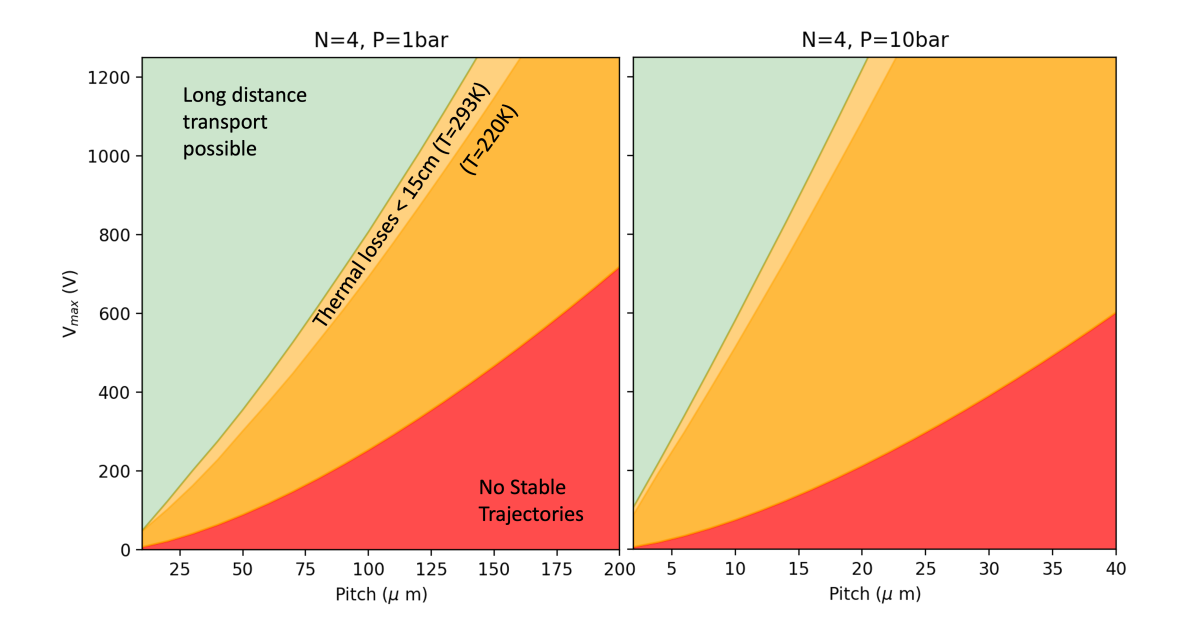


Figure 15: RF carpet stability regimes with fixed pressure and variable pitch. See text for more details. In the red region, the minimum of the pseudo-potential is not above the carpet surface. In the yellow regions, ions travel less than 15 cm on average at the two tested temperatures. The green region covers the parameter values where ions travel more than 15 cm on average at 293 K. Due to the rapid threshold-like form of the transport efficiency, the regions for 50 cm average travel are only different by a few percent in RF voltage.

Using this newly validated method for analytic modeling of RF carpet transport, the operating conditions required for transport of barium ions in xenon gas at pressures of 1–10 bar have been evaluated. If RF carpets can be operated with high transport efficiency in this regime it would enable ion collection from large volumes of xenon gas, which may prove to be a key ingredient in addressing the presently unsolved problem of ion concentration to sensors for barium tagging.

Our calculations show that stable ion motion over conventionally available RF carpets based on single layer PCBs on kapton appears viable up to 1 atmosphere of pressure. At this operating pressure, commercially available PCB manufacturing technologies [56] can be used to produce RF carpet structures with pitches of order 50 μ m on 30 cm diameter scales which would likely be able to support the required maximum driving voltage of $V_{max} \sim 350$ V. Construction of devices to operate at 10 bar of pressure, on the other hand, appears far more challenging. A structure with at most 15 μ m pitch supporting at least V_{max} =800 V would likely be required. Such parameters have been demonstrably achieved in past devices for quantum information science applications using nano-fabrication at single-chip scales [32, 33, 34]. To our knowledge, however, no device with such a fine feature size has been produced on the tens-of-centimeter scale required for this application. Since 300 mm is a standard wafer size in CMOS processing [62], with 450 mm under development [62], there is reason to be hopeful that such a device may be realizable with existing manufacturing techniques, though its demonstration will require considerable R&D. RF carpet devices operable in high pressures that may be realized in this way would likely find other important applications beyond double beta decay searches.

Experimental work on RF carpets for neutrinoless double beta decay detectors is currently underway within the NEXT collaboration. A near-term goal is to fabricate a 15 μ m pitch etched metal-on-sapphire RF carpet at 5 cm scale and demonstrate its performance for ion transport in xenon gas. Success in this endeavor may illuminate a path toward RF carpets operable in new pressure regimes, potentially providing a new method of ion concentration for barium daughter ion tagging following neutrinoless double beta decay.

Acknowledgements:

We thank Ben Smithers and Jackie Baeza Rubio for careful proof-reading, and Yuan Mei for thoughtful suggestions which were incorporated into the draft. The University of Texas at Arlington NEXT group is supported by the Department of Energy under Early Career Award number DE-SC0019054 (BJPJ), by Department of Energy Award DE-SC0019223 (DRN), the National Science Foundation under award number NSF CHE 2004111 (FWF), and the Robert A Welch Foundation, Y-2031-20200401 (FWF). The

NEXT Collaboration acknowledges support from the following agencies and institutions: the European 701 Research Council (ERC) under the Advanced Grant 339787-NEXT; the European Union's Framework 702 Programme for Research and Innovation Horizon 2020 (2014–2020) under the Grant Agreements No. 703 674896, 690575 and 740055; the Ministerio de Economía y Competitividad and the Ministerio de Ciencia, Innovación y Universidades of Spain under grants FIS2014-53371-C04, RTI2018-095979, the Severo Ochoa 705 Program grants SEV-2014-0398 and CEX2018-000867-S, and the María de Maeztu Program MDM-706 2016-0692; from Fundacion Bancaria la Caixa (ID 100010434), grant code LCF/BQ/PI19/11690012; the Generalitat Valenciana of Spain under grants PROMETEO/2016/120 and SEJI/2017/011; the Portuguese FCT under project PTDC/FIS-NUC/2525/2014 and under projects UID/FIS/04559/2020 to fund the 709 activities of LIBPhys-UC; the Pazy Foundation (Israel) under grants 877040 and 877041; the US Department 710 of Energy under contracts number DE-AC02-06CH11357 (Argonne National Laboratory), DE-AC02-711 07CH11359 (Fermi National Accelerator Laboratory), DE-FG02-13ER42020 (Texas A&M). DGD acknowledges support from the Ramón y Cajal program (Spain) under contract number RYC-2015-18820. JM-A 713 acknowledges support from Fundación Bancaria la Caixa (ID 100010434), grant code LCF/BQ/PI19/11690012, and from the Plan GenT program of the Generalitat Valenciana, grant code CIDEGENT/2019/049. Finally, we are grateful to the Laboratorio Subterráneo de Canfranc for hosting and supporting the NEXT experiment. 717

Appendix: The Dehmelt potential

719

721

722

723

724

725

727

728

729

732

733

734

The levitating force in RF carpets operated with a purely periodic field strength can be understood in terms of a Dehmelt potential, the same basic principle operational in Paul traps. The Dehmelt potential is an interesting and not totally intuitive effect, where an RF field which averages to zero over a cycle everywhere at each point in space can still exert an overall force on a particle when averaged over time, if it is spatially inhomogeneous. Consider an electric field with position \vec{r} dependence of the form:

$$\vec{E}\left[\vec{r},t\right] = \vec{E}_0\left[\vec{r}\right]\cos\Omega t\tag{35}$$

This field has a position dependence and fast time dependence at the RF frequency Ω . We consider three cases of particle motion. First, a ballistic (vacuum-like) motion, and then a fully viscous (high pressure gas-like) motion, and finally, something in between (which it turns out is the most relevant case for operation RF carpets).

Fully Ballistic Case: A particle moving in this field in a ballistic, non-viscous setting obeys equation of motion:

$$m\ddot{r} = q\vec{E}\left[\vec{r}(t), t\right] \cdot \vec{r} = q\vec{E}_0\left[\vec{r}(t)\right] \cos\left(\Omega t\right). \tag{36}$$

We seek solutions defined by having a periodic "micro-motion" $\vec{\xi}$ on the RF timescale, superposed on a "macro-motion" \vec{z} on slower timescales:

$$\vec{r}(t) = \vec{z}(t) + \vec{\xi}(t). \tag{37}$$

Substituting this expression into Eq. 36 we find:

$$m\ddot{\vec{z}} + m\ddot{\vec{\xi}} = q\vec{E}_0 \left[\vec{z} + \vec{\xi} \right] \cos(\Omega t). \tag{38}$$

Two approximations allow us to proceed to solve for the micro-motion. First, we approximate that the cycles defined by the micro-motion take place over regions where the electric field does not vary sustantially, so that $\vec{E}_0 \left[\vec{z} + \vec{\xi} \right] \sim \vec{E}[\vec{z}]$. Second, we approximate that the timescales associated with the micro-motion, $\tau \sim 1/\Omega$ are much faster than the timescales associated with the macro-motion so $\ddot{z}_i \ll \ddot{\xi}_i$ for all i. Then we obtain an equation for the micro-motion alone:

$$m\vec{\xi} = q\vec{E}_0[\vec{z}]\cos(\Omega t) \tag{39}$$

This has the periodic solution:

$$\vec{\xi} = \frac{q}{m\Omega^2} \vec{E}_0 \left[\vec{z} \right] \cos \left(\Omega t \right) \tag{40}$$

To solve for the macro-motion, we return to the equation of motion and expand $\vec{E}[\vec{r}]$ to first order in $\vec{\xi}$:

$$m\vec{z} + q\vec{E}_0[\vec{z}]\cos(\Omega t) = q\left(1 + \vec{\xi}(t)\cdot\nabla\right)\vec{E}_0[\vec{z}]\cos(\Omega t)$$
(41)

Substituting the solution for the micro-motion:

$$m\ddot{\vec{z}} = \frac{q^2}{m\Omega^2} \left(\vec{E}_0 \cdot \nabla \right) \vec{E}_0 \cos^2(\Omega t) \tag{42}$$

Averaging over a period in Ωt to find the slow-timescale behavior:

$$\langle \ddot{\vec{z}} \rangle = \frac{q^2}{m\Omega^2} \left\langle \left(\vec{E}_0 \cdot \nabla \right) \vec{E}_0 \cos^2 \left(\Omega t \right) \right\rangle = \frac{1}{2} \frac{q^2}{m^2 \Omega^2} \left(\vec{E}_0 \cdot \nabla \right) \vec{E}_0 \tag{43}$$

If the E field is homogenous then $\nabla \vec{E} = 0$ and there is no macro-motion. However, an interesting situation is apparent when $\nabla \vec{E} \neq 0$. Now there is a non-zero force, after time averaging, even though the RF field at each point in space averages to zero.

$$\langle \ddot{\vec{z}} \rangle = \frac{q^2}{4m^2\Omega^2} \nabla \left(E_0^2 \left[\vec{z} \right] \right) \tag{44}$$

This can be compactly written:

$$\langle \ddot{\vec{z}} \rangle = q \nabla V \tag{45}$$

With V the effective potential:

$$V = \frac{qE_0^2[\vec{z}]}{4m^2\Omega^2} \tag{46}$$

It is this repulsive potential that acts to levitate ions over any RF structures that have non-uniform and time varying electric fields near their surfaces.

Fully Viscous Case: We can also consider a scenario with a viscous motion, as we would expect in very high pressure environments. We now take as starting point the viscous equation of motion:

$$\dot{\vec{r}} = q\mu \vec{E}_0 \left[\vec{r}(t) \right] \cos \left(\Omega t \right) \tag{47}$$

Here μ is the mobility and the dynamical term on the left involves only one time derivative. Again we seek solutions defined by a micro-motion $\vec{\xi}$ on the RF timescale superposed on a macro-motion \vec{z} on slower timescales. Solving for the micro-motion using the same approximations as before yields:

$$\vec{\xi}(t) = \frac{\mu q}{\Omega} \vec{E}_0 \left[\vec{z} \right] \sin \left(\Omega t \right) \tag{48}$$

And so:

748

751

755

760

761

766

$$\dot{\vec{z}} = \frac{\mu^2 q^2}{\Omega} \left(\vec{E}_0 \cdot \nabla \right) \vec{E}_0 \frac{1}{2} \sin(2\Omega t) \tag{49}$$

In this case, however, when time averaging over an oscillation we find there is no longer a levitating force:

$$\langle \dot{\vec{z}} \rangle = 0 \tag{50}$$

Thus is a scenario where the ion motion is trully viscous over the RF timescale, ion levitation using RF fields is not possible.

Intermediate case: It would be an over-simplification to state that ions exhibit viscous motion in high pressure gases but ballistic motion in low pressure ones. When we consider ion swarms propelled by DC drift fields, it is understood that the particles are subject to viscous motion on the long timescales required to cross a particle detector. However, they still accelerate ballistically between collisions with gas atoms. The ion motion on a microscopic scale thus exhibits both ballistic and viscous elements.

The full equation of motion in the presence of both ballistic and viscous terms can be written as:

$$m\ddot{\vec{r}} + \frac{q}{\mu}\dot{\vec{r}} = q\vec{E}_0\left[\vec{r}(t)\right]\cos\left(\Omega t\right) \tag{51}$$

Following the same approach as before we can solve for the fast micro-motion:

$$m\Omega^2 \ddot{\vec{\xi}} + \frac{q}{\mu} \Omega \dot{\vec{\xi}} = q \vec{E}_0 \left[\vec{r}(t) \right] \cos \left(\Omega t \right) \tag{52}$$

The solution to this second order differential equation is a damped, periodic motion with a phase shift:

$$\vec{\xi} = \frac{q}{m\Omega} \frac{\vec{E}_0}{\sqrt{\Omega^2 + D^2}} \cos(\Omega t + \beta) \qquad \tan \beta = \frac{D^2}{\Omega^2}$$
 (53)

Above we have introduced the "Damping factor":

$$D = \frac{e}{m\mu} \tag{54}$$

The ballistic limit corresponds to $\tan \beta \to 0$ so $\beta \to 0$ and the micro-motion totally in phase with the RF; whereas the viscous limit corresponds to $\tan \beta \to \infty$ so $\beta \to \pi$ and the micro-motion totally out of phase with the RF. This principle can be used to understand where the effective force from the Dehmelt potential comes from, by considering the reinforcing action (or lack of) of the non-uniform electric field at different points in the micro-cycle. Fig. 16 illustrates this principle.

Proceeding with a derivation of the macro-motion:

$$m\langle \ddot{\vec{z}}\rangle + \frac{q}{\mu}\langle \dot{\vec{z}}\rangle = \frac{q}{4m\Omega} \frac{1}{\sqrt{\Omega^2 + D^2}} \left(\vec{E}_0 \cdot \nabla \right) \vec{E}_0 \left\langle \cos(\Omega t + \beta) \cos(\Omega t) \right\rangle \tag{55}$$

A trigonometric identity helps us with the time average on the right, and only the first term survives being time-averaged:

$$\langle \cos(\Omega t + \beta) \cos(\Omega t) \rangle = \langle (\cos(\Omega t) \cos(\beta) - \sin(\Omega t) \sin(\beta)) \cos(\Omega t) \rangle$$
(56)

$$=\frac{1}{2}\cos\beta.\tag{57}$$

We can also write this as:

772

773

778

780

781

784

786

788

789

791

792

793

794

795

796

$$\cos \beta = \frac{1}{\sqrt{1 + \tan^2 \theta}} = \frac{\Omega}{\sqrt{\Omega^2 + D^2}} \tag{58}$$

Thus our equation of motion has become:

$$m\langle \ddot{\vec{z}}\rangle + \frac{q}{\mu}\langle \dot{\vec{z}}\rangle = \frac{q}{4m} \frac{E_0}{\Omega^2 + D^2} \nabla \left(E_0^2 \left[\vec{z} \right] \right) \tag{59}$$

The statement that on timescales associated with macro-motion the dynamics are viscous corresponds to the condition $\frac{q}{\mu} \langle \dot{z} \rangle \gg m \langle \ddot{z} \rangle$. In this scenario we find:

$$\frac{q}{\mu}\langle \dot{\vec{z}} \rangle = \nabla V \tag{60}$$

$$V = \frac{q}{4m} \frac{1}{\Omega^2 + D^2} E_0^2 [\vec{z}]$$
 (61)

As required. We see then that interestingly, even in the extremely viscous limit where $D \gg \Omega$, a Dehmelt potential remains active, though suppressed by the damping factor.

References

- T. Kim, A. V. Tolmachev, R. Harkewicz, D. C. Prior, G. Anderson, H. R. Udseth, R. D. Smith, T. H. Bailey, S. Rakov, J. H. Futrell, Design and implementation of a new electrodynamic ion funnel, Analytical chemistry 72 (10) (2000) 2247–2255.
- [2] S. A. Shaffer, K. Tang, G. A. Anderson, D. C. Prior, H. R. Udseth, R. D. Smith, A novel ion funnel for focusing ions at elevated pressure using electrospray ionization mass spectrometry, Rapid communications in mass spectrometry 11 (16) (1997) 1813–1817.
- [3] P. Schury, M. Wada, Y. Ito, F. Arai, D. Kaji, S. Kimura, K. Morimoto, H. Haba, S. Jeong, H. Koura, et al., Status of the low-energy super-heavy element facility at riken, Nuclear Instruments and Methods in Physics Research Section B: Beam Interactions with Materials and Atoms 376 (2016) 425–428.
- [4] G. Savard, S. Baker, C. Davids, A. Levand, E. Moore, R. Pardo, R. Vondrasek, B. Zabransky, G. Zinkann, Radioactive beams from gas catchers: The caribu facility, Nuclear Instruments and Methods in Physics Research Section B: Beam Interactions with Materials and Atoms 266 (19-20) (2008) 4086–4091.

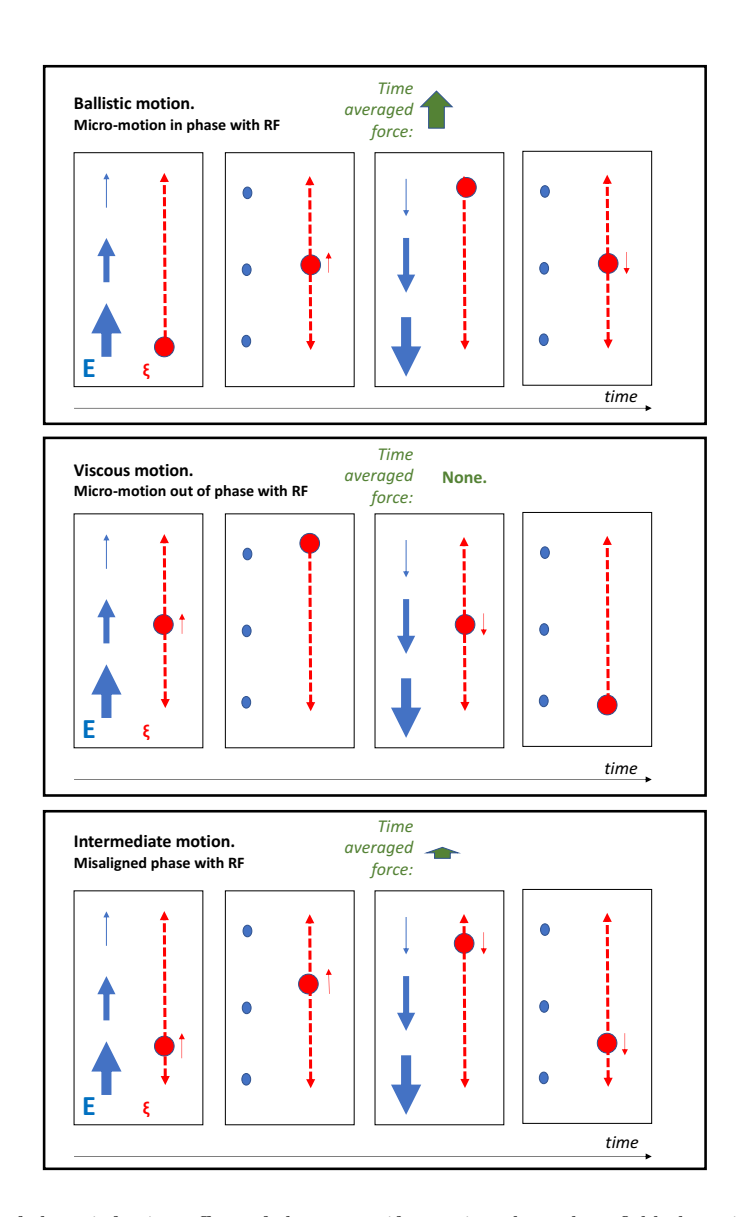


Figure 16: Illustration of the reinforcing effect of the non-uniform, time-dependent field that gives rise to the Dehmelt potential in ballistic and semi-ballistic but not in viscous motion.

- W. Paul, Electromagnetic traps for charged and neutral particles, Reviews of modern physics 62 (3) (1990) 531. 797
- H. G. Dehmelt, Radiofrequency spectroscopy of stored ions i: Storage, in: Advances in atomic and molecular physics, 798 Vol. 3, Elsevier, 1968, pp. 53–72.
- S. Schwarz, Rf ion carpets: The electric field, the effective potential, operational parameters and an analysis of stability, 800 International Journal of Mass Spectrometry 299 (2-3) (2011) 71-77. 801
 - G. Bollen, "ion surfing" with radiofrequency carpets, International Journal of Mass Spectrometry 299 (2-3) (2011) 131 - 138.
 - F. Arai, Y. Ito, M. Wada, P. Schury, T. Sonoda, H. Mita, Investigation of the ion surfing transport method with a circular rf carpet, International Journal of Mass Spectrometry 362 (2014) 56 - 58. doi:http://dx.doi.org/10.1016/ i.iims.2014.01.005.
 - ${\rm URL\ http://www.sciencedirect.com/science/article/pii/S1387380614000098}$

802

803

804

805

806

807

- [10] M. Brodeur, A. Gehring, G. Bollen, S. Schwarz, D. Morrissey, Experimental investigation of the ion surfing transport 808 method, International Journal of Mass Spectrometry 336 (2013) 53-60. 809
- 810 A. Gehring, M. Brodeur, G. Bollen, D. Morrissey, S. Schwarz, Research and development of ion surfing {RF} carpets for the cyclotron gas stopper at the {NSCL}, Nuclear Instruments and Methods in Physics Research Section B: Beam 811 Interactions with Materials and Atoms 376 (2016) 221 - 224, proceedings of the {XVIIth} International Conference 812 on Electromagnetic Isotope Separators and Related Topics (EMIS2015), Grand Rapids, MI, U.S.A., 11-15 May 2015. 813 doi:https://doi.org/10.1016/j.nimb.2016.02.012. 814 815
 - ${\rm URL\ http://www.sciencedirect.com/science/article/pii/S0168583X16001294}$
- L. Querci, V. Varentsov, D. Günther, B. Hattendorf, An rf-only ion funnel interface for ion cooling in laser ablation 816 time of flight mass spectrometry, Spectrochimica Acta Part B: Atomic Spectroscopy 146 (2018) 57–68. 817
- M. Ranjan, S. Purushothaman, T. Dickel, H. Geissel, W. Plaß, D. Schäfer, C. Scheidenberger, J. Van de Walle, 818 H. Weick, P. Dendooven, New stopping cell capabilities: Rf carpet performance at high gas density and cryogenic 819 operation, EPL (Europhysics Letters) 96 (5) (2011) 52001. 820
- A. D. Appelhans, D. A. Dahl, Simion ion optics simulations at atmospheric pressure, International Journal of Mass 821 Spectrometry 244 (1) (2005) 1–14. 822
- M. K. Moe, New approach to the detection of neutrinoless double beta decay, Physical Review C44 (1991) 931–934. 823 doi:10.1103/PhysRevC.44.931. 824
- 825 I. Rivilla, B. Aparicio, J. M. Bueno, D. Casanova, C. Tonnelé, Z. Freixa, P. Herrero, C. Rogero, J. I. Miranda, R. M. 826 Martínez-Ojeda, et al., Fluorescent bicolour sensor for low-background neutrinoless double β decay experiments, Nature 583 (7814) (2020) 48-54. 827
- E. Bainglass, B. Jones, F. Foss Jr, M. Huda, D. Nygren, Mobility and clustering of barium ions and dications in 828 high-pressure xenon gas, Physical Review A 97 (6) (2018) 062509. 829
- J. C. B. Medina, Mobility And Fluorescence of Barium ions in Xenon Gas for the EXO Experiment, Ph.D Thesis 830 (2014).831
- B. Jones, A. McDonald, D. Nygren, Single molecule fluorescence imaging as a technique for barium tagging in 832 neutrinoless double beta decay, Journal of Instrumentation 11 (12) (2016) P12011. 833
- A. McDonald, B. Jones, D. Nygren, C. Adams, V. Álvarez, C. Azevedo, J. Benlloch-Rodríguez, F. Borges, A. Botas, 834 S. Cárcel, et al., Demonstration of single-barium-ion sensitivity for neutrinoless double-beta decay using single-molecule 835 fluorescence imaging, Physical review letters 120 (13) (2018) 132504. 836
- [21] B. Mong, S. Cook, T. Walton, C. Chambers, A. Craycraft, C. Benitez-Medina, K. Hall, W. Fairbank Jr, J. Albert, 837 D. Auty, et al., Spectroscopy of ba and ba+ deposits in solid xenon for barium tagging in nexo, Physical Review A 838 91 (2) (2015) 022505. 839
- C. Chambers, T. Walton, D. Fairbank, A. Craycraft, D. R. Yahne, J. Todd, A. Iverson, W. Fairbank, A. Alamre, 840 J. B. Albert, G. Anton, I. J. Arnquist, I. Badhrees, P. S. Barbeau, D. Beck, V. Belov, T. Bhatta, F. Bourque, J. P. 841 842 Brodsky, E. Brown, T. Brunner, A. Burenkov, G. F. Cao, L. Cao, W. R. Cen, S. A. Charlebois, M. Chiu, B. Cleveland, M. Coon, M. Côté, W. Cree, J. Dalmasson, T. Daniels, L. Darroch, S. J. Daugherty, J. Daughhetee, S. Delaquis, 843 A. Der Mesrobian-Kabakian, R. DeVoe, J. Dilling, Y. Y. Ding, M. J. Dolinski, A. Dragone, J. Echevers, L. Fabris, 844 J. Farine, S. Feyzbakhsh, R. Fontaine, D. Fudenberg, G. Gallina, G. Giacomini, R. Gornea, G. Gratta, E. V. Hansen, 845 M. Heffner, E. W. Hoppe, J. Hößl, A. House, P. Hufschmidt, M. Hughes, Y. Ito, A. Jamil, C. Jessiman, M. J. Jewell, 846 X. S. Jiang, A. Karelin, L. J. Kaufman, D. Kodroff, T. Koffas, S. Kravitz, R. Krücken, A. Kuchenkov, K. S. Kumar, 847 Y. Lan, A. Larson, D. S. Leonard, G. Li, S. Li, Z. Li, C. Licciardi, Y. H. Lin, P. Lv, R. MacLellan, T. Michel, B. Mong, 848 D. C. Moore, K. Murray, R. J. Newby, Z. Ning, O. Njoya, F. Nolet, O. Nusair, K. Odgers, A. Odian, M. Oriunno, 849 J. L. Orrell, G. S. Ortega, I. Ostrovskiy, C. T. Overman, S. Parent, A. Piepke, A. Pocar, J. F. Pratte, D. Qiu, 850 V. Radeka, E. Raguzin, T. Rao, S. Rescia, F. Retière, A. Robinson, T. Rossignol, P. C. Rowson, N. Roy, R. Saldanha, 851 S. Sangiorgio, S. Schmidt, J. Schneider, A. Schubert, K. Skarpaas, A. K. Soma, G. St-Hilaire, V. Stekhanov, T. Stiegler, 852 X. L. Sun, M. Tarka, T. Tolba, T. I. Totev, R. Tsang, T. Tsang, F. Vachon, B. Veenstra, V. Veeraraghavan, G. Visser, 853 J. L. Vuilleumier, M. Wagenpfeil, Q. Wang, J. Watkins, M. Weber, W. Wei, L. J. Wen, U. Wichoski, G. Wrede, 854
- S. X. Wu, W. H. Wu, Q. Xia, L. Yang, Y. R. Yen, O. Zeldovich, X. Zhang, J. Zhao, Y. Zhou, T. Ziegler, nEXO 855 Collaboration, Imaging individual barium atoms in solid xenon for barium tagging in nexo, Nature 569 (7755) (2019) 856 203-207. doi:10.1038/s41586-019-1169-4. 857
 - URL https://doi.org/10.1038/s41586-019-1169-4
- D. R. Nygren, Detecting the barium daughter in 136xe $0-\nu\beta\beta$ decay using single-molecule fluorescence imaging 859 techniques, in: Journal of Physics: Conference Series, Vol. 650, IOP Publishing, 2015, p. 012002. 860
- D. Sinclair, E. Rollin, J. Smith, A. Mommers, N. Ackeran, B. Aharmin, M. Auger, P. Barbeau, C. Benitez-Medina, 861 M. Breidenbach, et al., Prospects for barium tagging in gaseous xenon, in: Journal of Physics: Conference Series, Vol. 862 863 309, IOP Publishing, 2011, p. 012005.
- P. Thapa, I. Arnquist, N. Byrnes, A. Denisenko, F. Foss, B. Jones, A. McDonald, D. Nygren, K. Woodruff, Barium 864 chemosensors with dry-phase fluorescence for neutrinoless double beta decay, Scientific reports 9 (1) (2019) 1-13. 865
- [26] P. Thapa, N. K. Byrnes, A. A. Denisenko, J. X. Mao, A. D. McDonald, C. A. Newhouse, T. T. Vuong, K. Woodruff, K. Nam, D. R. Nygren, et al., Demonstration of selective single-barium ion detection with dry diazacrown ether 867 naphthalimide turn-on chemosensors, ACS sensors 6 (1) (2021) 192–202. 868
- [27] K. Twelker, S. Kravitz, E. Collaboration, et al., Barium tagging from nexo using resonance ionization spectroscopy,

Physics Procedia 61 (2015) 278-282. 870

896

- [28] T. Brunner, D. Fudenberg, V. Varentsov, A. Sabourov, G. Gratta, J. Dilling, R. DeVoe, D. Sinclair, W. Fairbank Jr, 871 J. B. Albert, et al., An rf-only ion-funnel for extraction from high-pressure gases, International Journal of Mass 872 Spectrometry 379 (2015) 110-120. 873
- B. Flatt, M. Green, J. Wodin, R. DeVoe, P. Fierlinger, G. Gratta, F. LePort, M. M. Diez, R. Neilson, K. O. A. 874 Pocar, E. Baussan, M. Breidenbach, R. Conley, W. M. Fairbank, Jr., J. Farine, K. Hall, D. Hallman, C. Hargrove, 875 M. Hauger, J. Hodgson, F. Juget, D. Leonard, D. Mackay, Y. Martin, B. Mong, A. Odian, L. Ounalli, A. Piepke, 876 C. Prescott, P. Rowson, K. Skarpaas, D. Schenker, D. Sinclair, V. Strickland, C. Virtue, J.-L. Vuilleuimier, J.-M. 877 Vuilleuimier, K. Wamba, P. Weber, A linear RFQ ion trap for the Enriched Xenon Observatory, Nuclear Instruments 878 and Methods in Physics Research Section A: Accelerators, Spectrometers, Detectors and Associated Equipment A578 879 (2007) 399-408. arXiv:0704.1646, doi:10.1016/j.nima.2007.05.123.
- K. Twelker, S. Kravitz, M. M. Díez, G. Gratta, W. Fairbank Jr, J. Albert, D. Auty, P. Barbeau, D. Beck, C. Benitez-881 Medina, et al., An apparatus to manipulate and identify individual ba ions from bulk liquid xe, Review of Scientific 882 Instruments 85 (9) (2014) 095114. 883
- S. Poteshin, A. Burykina, A. Adamov, A. Sysoev, Investigation by simulation of the rf carpets for the transport of ions 884 885 at atmospheric pressures, European Journal of Mass Spectrometry 26 (4) (2020) 274–280.
- R. C. Sterling, H. Rattanasonti, S. Weidt, K. Lake, P. Srinivasan, S. Webster, M. Kraft, W. K. Hensinger, Fabrication 886 and operation of a two-dimensional ion-trap lattice on a high-voltage microchip, Nature communications 5 (1) (2014) 887 1-6.
- [33] K. R. Brown, J. Chiaverini, J. M. Sage, H. Häffner, Materials challenges for trapped-ion quantum computers, Nature 889 Reviews Materials (2021) 1-14. 890
- K. K. Mehta, A. Eltony, C. Bruzewicz, I. Chuang, R. Ram, J. Sage, J. Chiaverini, Ion traps fabricated in a cmos 891 foundry, Applied Physics Letters 105 (4) (2014) 044103. 892
- [35] H. Lai, T. R. McJunkin, C. J. Miller, J. R. Scott, J. R. Almirall, The predictive power of simion/sds simulation software 893 for modeling ion mobility spectrometry instruments, International Journal of Mass Spectrometry 276 (1) (2008) 1-8. 894
- P. Jurčíček, L. Liu, H. Zou, Z. An, H. Xiao, Design, simulation and evaluation of improved air amplifier incorporating 895 an ion funnel for nano-esi ms, European Journal of Mass Spectrometry 20 (2) (2014) 143-154.
- M. Pauly, M. Sroka, J. Reiss, G. Rinke, A. Albarghash, R. Vogelgesang, H. Hahne, B. Kuster, J. Sesterhenn, K. Kern, 897 898 et al., A hydrodynamically optimized nano-electrospray ionization source and vacuum interface, Analyst 139 (8) (2014) 899
- D. Langridge, K. Giles, J. B. Hoyes, Simulation of ion motion in a travelling wave mobility separator using a hard-sphere 900 collision model, in: Proc. 56th ASMS Conference on Mass Spectrometry and Allied Topics, Denver, CO, 2008. 901
- C. Adams, V. Alvarez, L. Arazi, I. Arnquist, C. Azevedo, K. Bailey, F. Ballester, J. Benlloch-Rodriguez, F. Borges, 902 N. Byrnes, et al., Sensitivity of a tonne-scale next detector for neutrinoless double beta decay searches, arXiv preprint 903 arXiv:2005.06467 (2020). 904
- G. Savard, Large radio-frequency gas catchers and the production of radioactive nuclear beams, in: Journal of Physics: 905 Conference Series, Vol. 312, IOP Publishing, 2011, p. 052004. 906
- K. Woodruff, J. Baeza-Rubio, D. Huerta, B. Jones, A. McDonald, L. Norman, D. Nygren, C. Adams, V. Álvarez, 907 L. Arazi, et al., Radio frequency and dc high voltage breakdown of high pressure helium, argon, and xenon, Journal of 908 Instrumentation 15 (04) (2020) P04022. ana
- [42] B. J. P. Jones, XePA Project: Drift properties of helium added to xenon at 10 bar, http://www-910 hep.uta.edu/bjones/XePA/(2016). 911
- [43]R. Felkai, et al., Helium-Xenon mixtures to improve the topological signature in high pressure gas xenon TPCs, Nucl. 912 Instrum. Meth. A905 (2018) 82-90. arXiv:1710.05600, doi:10.1016/j.nima.2018.07.013. 913
- A. F. M. Fernandes, et al., Electroluminescence Yield in low-diffusion Xe-He gas mixtures (2019). arXiv:1906.03984. 914
- 915 A. D. McDonald, et al., Electron Drift and Longitudinal Diffusion in High Pressure Xenon-Helium Gas Mixtures, JINST 14 (08) (2019) P08009. arXiv:1902.05544, doi:10.1088/1748-0221/14/08/P08009. 916
- [46] 917 L. Rogers, B. Jones, A. Laing, S. Pingulkar, B. Smithers, K. Woodruff, C. Adams, V. Álvarez, L. Arazi, I. Arnquist, et al., Mitigation of backgrounds from cosmogenic 137 xe in xenon gas experiments using 3 he neutron capture, Journal 918 of Physics G: Nuclear and Particle Physics 47 (7) (2020) 075001. 919
- C. Henriques, C. Monteiro, D. González-Díaz, C. R. Azevedo, E. D. Freitas, R. Mano, M. Jorge, A. Fernandes, J. J. 920 Gómez-Cadenas, L. Fernandes, et al., Electroluminescence tpcs at the thermal diffusion limit, Journal of High Energy 921 Physics 2019 (1) (2019) 27. 922
- [48]D. González-Díaz, V. Álvarez, F. Borges, M. Camargo, S. Cárcel, S. Cebrián, A. Cervera, C. A. Conde, T. Dafni, 923 J. Díaz, et al., Accurate γ and mev-electron track reconstruction with an ultra-low diffusion xenon/tma tpc at 10 924 atm, Nuclear Instruments and Methods in Physics Research Section A: Accelerators, Spectrometers, Detectors and 925 Associated Equipment 804 (2015) 8-24. 926
- S. Cebrian, T. Dafni, E. Ferrer-Ribas, I. Giomataris, D. Gonzalez-Diaz, H. Gómez, D. Herrera, F. Iguaz, 927 I. Irastorza, G. Luzon, et al., Micromegas-tpc operation at high pressure in xenon-trimethylamine mixtures, Journal 928 of Instrumentation 8 (01) (2013) P01012. 929
- A. Trindade, P. Encarnação, J. Escada, A. Cortez, P. Neves, C. Conde, F. Borges, F. Santos, Experimental studies on 930 ion mobility in xenon-trimethylamine mixtures, Journal of Instrumentation 12 (07) (2017) P07007. 931
- A. Trindade, J. Escada, A. Cortez, F. Borges, F. Santos, C. Adams, V. Álvarez, L. Arazi, C. Azevedo, F. Ballester, 932 et al., Study of the loss of xenon scintillation in xenon-trimethylamine mixtures, Nuclear Instruments and Methods in 933 Physics Research Section A: Accelerators, Spectrometers, Detectors and Associated Equipment 905 (2018) 22–28. 934
- C. Henriques, E. D. Freitas, C. Azevedo, D. González-Díaz, R. Mano, M. Jorge, L. Fernandes, C. Monteiro, J. J. 935 936 Gómez-Cadenas, V. Álvarez, et al., Secondary scintillation yield of xenon with sub-percent levels of co2 additive for rare-event detection, Physics Letters B 773 (2017) 663-671. 937
- C. Azevedo, L. Fernandes, E. Freitas, D. Gonzalez-Diaz, F. Monrabal, C. Monteiro, J. Dos Santos, J. Veloso, J. Gomez-938 Cadenas, An homeopathic cure to pure xenon large diffusion, Journal of Instrumentation 11 (02) (2016) C02007.
- A. Bolotnikov, B. Ramsey, The spectroscopic properties of high-pressure xenon, Nuclear Instruments and Methods in 940 Physics Research A 396 (1997) 360-370. doi:10.1016/S0168-9002(97)00784-5. 941
- [55] P. Novella, B. Palmeiro, A. Simón, M. Sorel, C. Adams, P. Ferrario, G. Martínez-Lema, F. Monrabal, G. Zuzel, J. J.

- Gómez-Cadenas, et al., Measurement of radon-induced backgrounds in the next double beta decay experiment, Journal of High Energy Physics 2018 (10) (2018) 1–27.
- 945 [56] Averatek Corp, Game changer: 25-micron trace and space.
 946 URL http://www.averatekcorp.com/2020/09/07/hello-world
- 947 [57] M. Blain, R. Haltli, P. Maunz, C. Nordquist, M. Revelle, D. Stick, Hybrid mems-cmos ion traps for nisq computing,
 948 Quantum Science and Technology (2021).
- [58] S. Seidelin, J. Chiaverini, R. Reichle, J. J. Bollinger, D. Leibfried, J. Britton, J. Wesenberg, R. Blakestad, R. Epstein,
 D. Hume, et al., Microfabricated surface-electrode ion trap for scalable quantum information processing, Physical
 review letters 96 (25) (2006) 253003.
- [59] M. Niedermayr, K. Lakhmanskiy, M. Kumph, S. Partel, J. Edlinger, M. Brownnutt, R. Blatt, Cryogenic surface ion
 trap based on intrinsic silicon, New Journal of Physics 16 (11) (2014) 113068.
- 954 [60] Electron Microscopy Services, Kapton polyimide film tape.
 955 URL https://www.emsdiasum.com/microscopy/technical/datasheet/77708.aspx
- 956 [61] I. R. Regulations, C. II-Frequencies, Article 5 frequency allocations, Section IV—Table of Frequency Allocations (2012).
- 957 [62] Wikipedia, Wafer electronics.
- 958 URL https://en.wikipedia.org/wiki/Wafer_(electronics)